energies

MDPI

Review

The Relationship between Structure and Catalytic Activity-Stability of Non-Precious Metal-Based Catalysts towards Levulinic Acid Hydrogenation to γ-Valerolactone: A Review

Ying Yang *,†, Yuhang Sun † and Xinruo Luo

State Key Laboratory of Heavy Oil Processing, China University of Petroleum, Beijing 102249, China
* Correspondence: yyang@cup.edu.cn; Tel./Fax: +86-10-8973-4979
† These authors contributed equally to this work.

Abstract: Hydrogenation of levulinic acid (LA) to γ-valerolactone (GVL) is regarded as the bridge between bio-refinery and the traditional petroleum industry. In recent years, non-precious metal-based catalysts for LA hydrogenation to GVL have attracted much attention owing to their low cost and high efficiency. Metal-involving catalytic hydrogenation of LA is the rate-determining step in the production of GVL, and thus the active site structure of metal-based catalysts governs the overall catalytic performance. Herein, non-precious metal-based catalytic systems including Cu, Zr, Co and Ni are classified into single metal (M = Ni, Cu and Co), bimetallic (Cu–Ni, Ag–Ni, Cu–Co and Co–Zn), metal-heteroatom (M–O and M–N) and heterostructured ($CePO_4$/CoP_2 and Ni/NiO) catalysts according to the type of active site structure. The correlation of active site structure with catalytic activity is discussed emphatically, and its relationship with stability is also referred to in terms of strong metal–support interaction, bimetallic synergism, core–shell structure and heterojunction. This review provides an important guide for the rational design of high-performance non-precious metal-based catalysts for the LA-to-GVL process.

Keywords: non-precious metal; levulinic acid; γ-valerolactone; activity; stability; structure–property relationship

Citation: Yang, Y.; Sun, Y.; Luo, X. The Relationship between Structure and Catalytic Activity-Stability of Non-Precious Metal-Based Catalysts towards Levulinic Acid Hydrogenation to γ-Valerolactone: A Review. *Energies* **2022**, *15*, 8093. https://doi.org/10.3390/en15218093

Academic Editor: George Avgouropoulos

Received: 10 October 2022
Accepted: 28 October 2022
Published: 31 October 2022

1. Introduction

Non-renewable fossil resources are heavily relied upon in our society to produce fuels and chemicals which are utilized to improve people's lives and drive the global economy forward. However, environment deterioration and fossil resource depletion have forced us to look for renewable alternatives in order to realize the sustainable supply of fuels and chemicals [1–3]. Biomass is the only sustainable source of organic carbon on earth and it is considered to be the perfect equivalent of petroleum for the production of fuels, chemicals, and carbon-based materials [3,4]. Carbon dioxide emission is zero during the utilization of biomass, which would alleviate the greenhouse effect and facilitate sustainable development. More than 4 billion tons of biomass resources are produced each year, and the conversion of biomass-derived platform molecules into liquid fuels and high value-added chemicals is a key approach to realize sustainability [5,6]. Levulinic acid, as one of the most important platform molecules, can be obtained through the conversion of cellulose catalyzed by acids [7]. The hydrogenation of LA is considered a key process in the lignocellulose biorefinery industry [8], and the resulting GVL can be widely used for gasoline blender and solvent and can subsequently be processed to yield fuel additives and chemical intermediates [9–11]. In addition, GVL can also be converted into various alkanes, such as 1,4-pentanediol, 2-methyltetrahydrofuran, valeric biofuels and alkanes [12–16], as illustrated in Scheme 1. To date, several metal catalysts have been developed with the

goal of the hydrogenation of LA to GVL. Noble metal catalysts, including Ru [17], Ir [18], Pd [19] and Pt [20], have proven to be highly active and selective under mild reaction conditions. In the presence of noble metals, the keto functionality of LA is hydrogenated into the alcohol group to render 4-hydroxyvaleric acid, which is then dehydrated to GVL. However, the large-scale application of noble metal catalysts is restricted owing to their high cost and scarcity [21]. In recent years, advances in research have focused on the development of cheap and abundant non-precious metal-based catalysts (like Ni, Co, Cu, Fe and Zr). They have varied valences, exhibiting tunable physicochemical properties, and are expected to be superior to precious metal catalysts for the LA-to-GVL process [22]. These non-precious metal catalysts can accommodate H_2 [20], formic acid (FA) [23], and alcohols [24] as hydrogen sources.

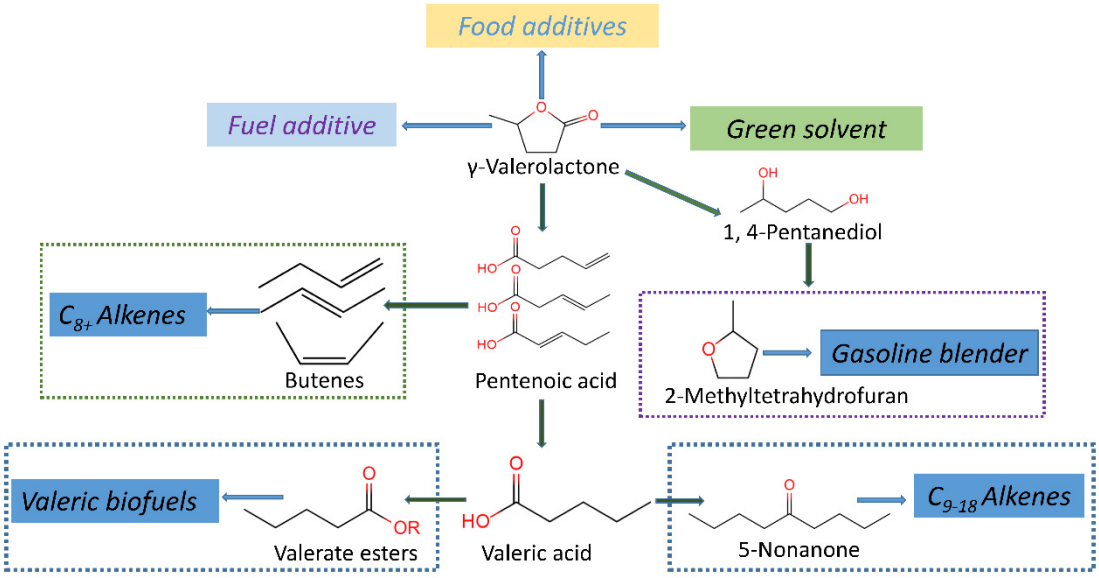

Scheme 1. Schematic illustration of GVL conversion to chemicals and fuels, and their applications.

Previous studies have primarily concentrated on the overall catalytic performance of non-precious metal-based catalysts by varying the reaction conditions [25]. For example, LA conversion and catalyst cycling have been improved by elevating the temperature and H_2 pressure or by prolonging the reaction time [26–28]. Nevertheless, optimization of reaction conditions but ignorance of active sites cannot afford excellent catalytic performance. Metal sites are intrinsically crucial to the catalytic performance, especially in governing the rate-determined hydrogenation step during GVL synthesis, whereas, variation of non-precious metals cannot improve the catalytic activity and stability significantly [29]. Current investigations are moving to active site construction and modulation, and efforts have been focused on the active site structure of metal catalysts towards LA hydrogenation. Single metal sites with high dispersion [30,31], bimetallic sites with synergism [32], heteroatom-doped and heterostructured sites with tunable electronic structure [33–35] have been developed, and the resulting catalysts exhibit remarkably improved LA conversion and cycling durability for the LA-to-GVL process. For example, both N-doped cobalt and heterostructured Ni/NiO have proven to be highly efficient for LA hydrogenation, and they can be cycled 10 times without significant loss of activity [33–35]. These observations strongly suggest that the active site structure is the core of a non-precious metal-based catalyst.

To the best of our knowledge, the types of metal catalysts (including precious and non-precious metals), biomass-derived feedstocks (LA and its esters, furfural, furfuryl alcohol, etc.), hydrogen sources (H_2, formic acid and alcohols) and support acidity have been summarized for LA hydrogenation [6,11,36–40]. However, there are not any reviews for the structure–property relationship of non-precious metal-based catalysts for LA hydrogena-

tion, though one would be highly desirable. In view of this, we summarize the influences of metal dispersion, loading, heteroatom doping, synergistic effect and heterojunction on the catalytic activity and stability of non-precious metal-based catalysts. Through in-depth discussion of the key issues above, it is expected that the rational design of an active site structure would be strengthened by metal catalysts, facilitating the performance improvement of non-precious metal-based catalysts towards biomass conversion.

2. Reaction Mechanism

Exploration of the reaction mechanisms of the LA-to-GVL process is the prerequisite to design high-performance non-precious metal-based catalysts. In general, GVL can be produced by the hydrogenation of LA via multiple pathways with different hydrogen sources (Figure 1). A reasonable Langmuir–Hinshelwood mechanism in which the surface reaction is controlled by two adsorbed molecules has been deduced for the conversion of LA to GVL over heterostructured Ni/NiO and $CePO_4/CoP_2$ with dual active sites or a single active site with N dopants [35,41,42]. Based on the Langmuir–Hinshelwood mechanism, LA adsorption and H_2 activation are initiated on alkaline moieties and metallic species, and the surface reaction occurs subsequently to produce GVL. When H_2 molecule is utilized as the H-donor, two possible reaction pathways are proposed, which depend on the active sites and the controlling conditions employed [43]. Temperature plays a decisive role in the tendency of reaction pathways among the influencing factors that determine the reaction mechanism. At a lower temperature, the metal-catalyzed hydrogenation is carried out first, and LA is hydrogenated to 4-hydroxyvaleric acid (4-HVA), which can subsequently be dehydrated to generate GVL [44]. This pathway is thermodynamically preferred and has proven to be kinetically dominated at a low temperature. The second pathway involves endothermic dehydration of LA catalyzed by acids at high temperatures (>180 ^oC) to render α-angelica lactone by intramolecular esterification, which is subsequently hydrogenated to GVL [45]. Moreover, LA hydrogenation is reported to proceed through 4-HVA intermediate in the liquid phase, whereas AL is formed when hydrogenation occurs in the vapor phase. No α-angelica lactone can be found for LA hydrogenation in the absence of solvents. In the two pathways depicted, hydrogenation is influenced by the activity of non-precious metals, while dehydration depends on the reaction medium. Metal-catalyzed hydrogenation is crucial for GVL synthesis, whereas the promoting effect of support acidity must be recognized. It is reported that enhanced support acidity can facilitate LA conversion (via an accelerated 4-HVA generation) or GVL formation (via an improved AL conversion) [46,47]. A satisfactory GVL yield can be achieved under mild conditions when specific catalysts with suitable support acidity are applied [48,49]. However, at an elevated temperature, LA dehydration is facilitated to produce α-angelica lactone, which polymerizes on acidic sites to form coke, resulting in severe deactivation of catalysts.

The hydrolysis of cellulose to LA can produce an equimolar amount of formic acid (FA), which can reduce LA to GVL without extra hydrogen sources. The FA/LA catalytic system involves two processes, that is, selective decomposition of FA and LA hydrogenation. The selective degradation of FA is of great importance, since the decomposition degree determines the hydrogen supply efficiency. Two kinetic pathways exist when FA acts as the hydrogen donor: (1) dehydrogenation of FA to form H_2 and CO_2 and (2) dehydration of FA to form H_2O and CO [50]. The former is desired, because not only can it produce hydrogen donor, but it can also prevent catalyst poisoning caused by CO. Undoubtedly, non-precious metal-based catalysts capable of simultaneous FA decomposition and LA hydrogenation are essential for the FA/LA catalytic system. It is noted that competitive adsorption between FA and LA over heterogeneous catalysts was demonstrated, and trace LA was converted before FA was fully decomposed. It is found that FA decomposes first to generate hydrogen as metal catalysts involved, while LA hydrogenation only occurred in FA-derived hydrogen atmosphere. However, the use of FA entails the drawbacks of requiring a high temperature and leading to a low GVL yield.

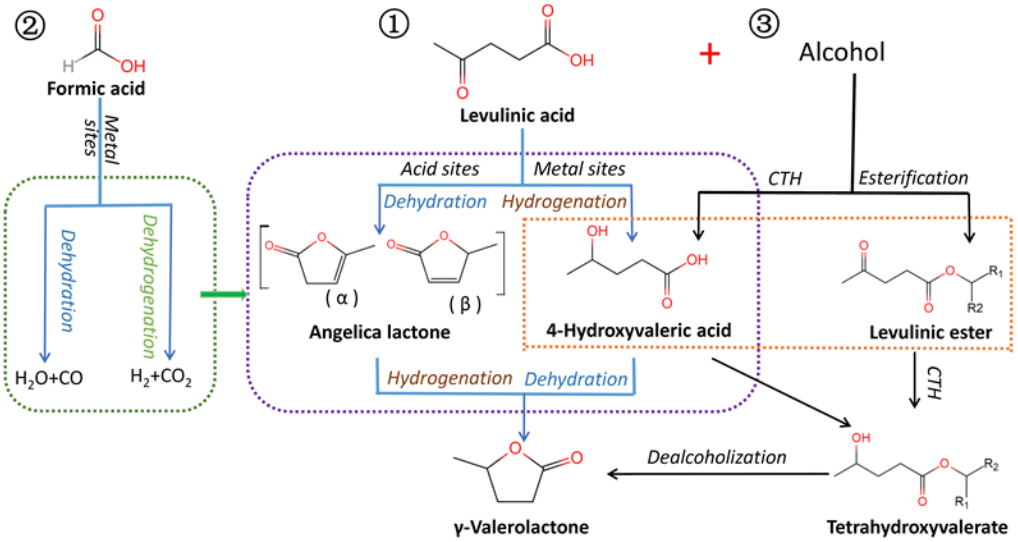

Figure 1. Reaction pathways for LA hydrogenation to GVL when different hydrogen donors are involved.

Additionally, alcohols can also provide cheaper and safer hydrogen donors for LA hydrogenation to GVL. With acid sites, LA was converted to alkyl levulinate, which further evolved into GVL via the catalytic transfer hydrogenation (CTH) [24]. From a mechanical point view, LA hydrogenation to GVL is a bifunctional catalytic process, and both metal-catalyzed hydrogenation and acid-involved dealcoholization contribute to GVL formation. It is noteworthy that metal and acid sites work cooperatively and are strongly related to the property of supports. Typically, support structure affects the dispersion and particle size of active metals, thus influencing the hydrogenation efficiency. Also, the acid sites derived from the supports are demonstrated to exert potential effects on the esterification or lactonization. Alcohols have proven to be superior to H_2 under mild conditions. As compared to primary and secondary alcohols including 2-propanol, 2-butanol and cyclohexanol, they are more promising and can deliver 100% LA conversion and high GVL yield (92–99%) [24]. On the other hand, CTH via the Meerwein–Ponndorf–Verley (MPV) reaction is viable for the hydrogenation of LA over non-precious metal-based catalysts. This reaction has proven to be highly chemo-selective for the reduction of carbonyl groups under mild conditions and with other functional groups like C=C bond [51]. The LA accepts hydrogen from alcohols to form 4-hydroxypentanoic acid or undergoes transesterification which ultimately leads to the formation of GVL; the alcohol involved in the reaction is transformed into ketone. The CTH process is a better alternative for the scalable production of GVL, since the reaction proceeds under milder conditions, and the alcohol is used as the greener H–donor. In addition, liquid-phase MPV reduction is performed at the boiling point of alcohol and ambient pressure, which makes the process environmentally friendly and cost-effective.

In terms of the hydrogenation mechanism above, the metal-catalyzed hydrogenation is crucial to facilitate LA transformation (generation of 4-HVA) or GVL formation (conversion of AL). Therefore, the correlation of the metal site structure with LA hydrogenation needs to be thoroughly investigated. For a kinetic process with non-precious metal-based catalysts involved, different active sites may lead to varied reaction mechanisms. In the following sections, non-precious metal catalytic systems with different active structures are summarized, and their influence on catalytic activity and stability will be discussed in detail.

3. Structure–Activity Relationship

Heterogeneous catalysts with different non-precious metal active sites have attracted significant attention from researchers for GVL synthesis, because they are easily separated

and are beneficial for reactors and the environment. In this section, the performance of the non-precious metal-based catalysts, including single, bimetallic, heteroatom-doped and heterostructural metal catalysts, as well as their active site structure, are discussed for the hydrogenation of LA to GVL. The reaction condition and the catalytic performance are summarized in Tables 1–4.

3.1. Single Metal Catalyst

For single metal catalysts, the acid density and the size of metal nanoparticles are crucial for their catalytic performance. It has been shown that the total Lewis and Brönsted acidity can be tailored by varying the metal loading, and thus the catalytic performance of metal catalysts can be tuned. Kumar et al. [52] developed a Ni/TiO_2 catalyst with various Ni loadings (5.0, 10.0, 15.0, 20.0 and 30.0 wt%) using a deposition–precipitation method (Table 1, entries 1–5). The optimized 20 wt.% Ni/TiO_2 catalyst delivers 99.9% LA conversion and 99.5% GVL selectivity. It was found that the selectivity toward GVL depends on the acid density of catalysts. For example, the number of Lewis acid sites (LAS) is higher for 20 wt.% Ni/TiO_2 compared to that for 5 wt.% Ni/TiO_2, and vice versa for the number of Brönsted acid sites (BAS). The relative ratio of the peak intensity measured by Kubelka–Munk correction gives the following relationship: LAS_{20NiT}/LAS_{5NiT} = 5.41 and BAS_{20NiT}/BAS_{5NiT} = 0.41 (Figure 2a). A comparative catalytic test for 20 wt.% Ni/TiO_2 and 5 wt.% Ni/TiO_2 shows that the Lewis acid is helpful in improving the selectivity toward GVL, while the Brönsted acid can facilitate the ring opening of GVL to form valeric acid and hydrocarbon. Moreover, the correlation between GVL ring opening products and Ni crystallite size is also established. As the loading of Ni is increased from 5 to 20 wt%, the Ni crystallite size is elevated from 34.1 to 67.4 nm, and the selectivity toward GVL increases from 87.6 to 99.1%. The formation of ring opening products is restrained, and the moderate crystallite size of −65 nm (for 20 wt.% Ni/TiO_2) is found to be optimum for the required GVL selectivity (Figure 2b). As for Ni catalysts, the metal dispersion and acidity are support-dependent. As illustrated, a series of Ni catalysts with different supports (including MgO, Al_2O_3 and MgO-Al_2O_3) were prepared using a co-precipitation method (Table 1, entries 6–10) [31]. It was found that Ni/MgO-Al_2O_3 could contribute to a higher dispersion of Ni and deliver complete conversion of LA and 99% selectivity toward GVL, as compared to Ni/MgO and Ni/Al_2O_3. Other metal oxides, such as SiO_2, ZrO_2, TiO_2 and ZnO, were also used as supports to prepare Ni catalysts through a wet impregnation method [53]. A maximum GVL productivity of 0.8506 $kg_{GVL}kg_{catalyst}{}^{-1}h^{-1}$ was obtained over Ni/SiO_2 catalyst that contains 30 wt.% of Ni. Compared to other Ni catalysts, a higher Ni dispersion (7.6%) and smaller Ni nanoparticles (13.3 nm) were detected for Ni/SiO_2 (Figure 2c). These features are beneficial for the controlled synthesis of 4-hydroxyvaleric acid, which is subsequently converted to GVL through dehydration cyclization. Nevertheless, compared to Ni/SiO_2, it was found that Ni/Al_2O_3, Ni/ZnO and Ni/ZrO_2 with more acid sites deliver a lower yield of GVL due to the formation of larger Ni particles (15.6–65.5 nm) with an inferior Ni dispersion (1.5–6.5%). The Ni/SiO_2, with a moderate acidity (Figure 2d), showed better performance for LA hydrogenation to GVL. These results demonstrate that the dispersion and particle size of Ni nanoparticles are crucial in determining the overall GVL synthesis.

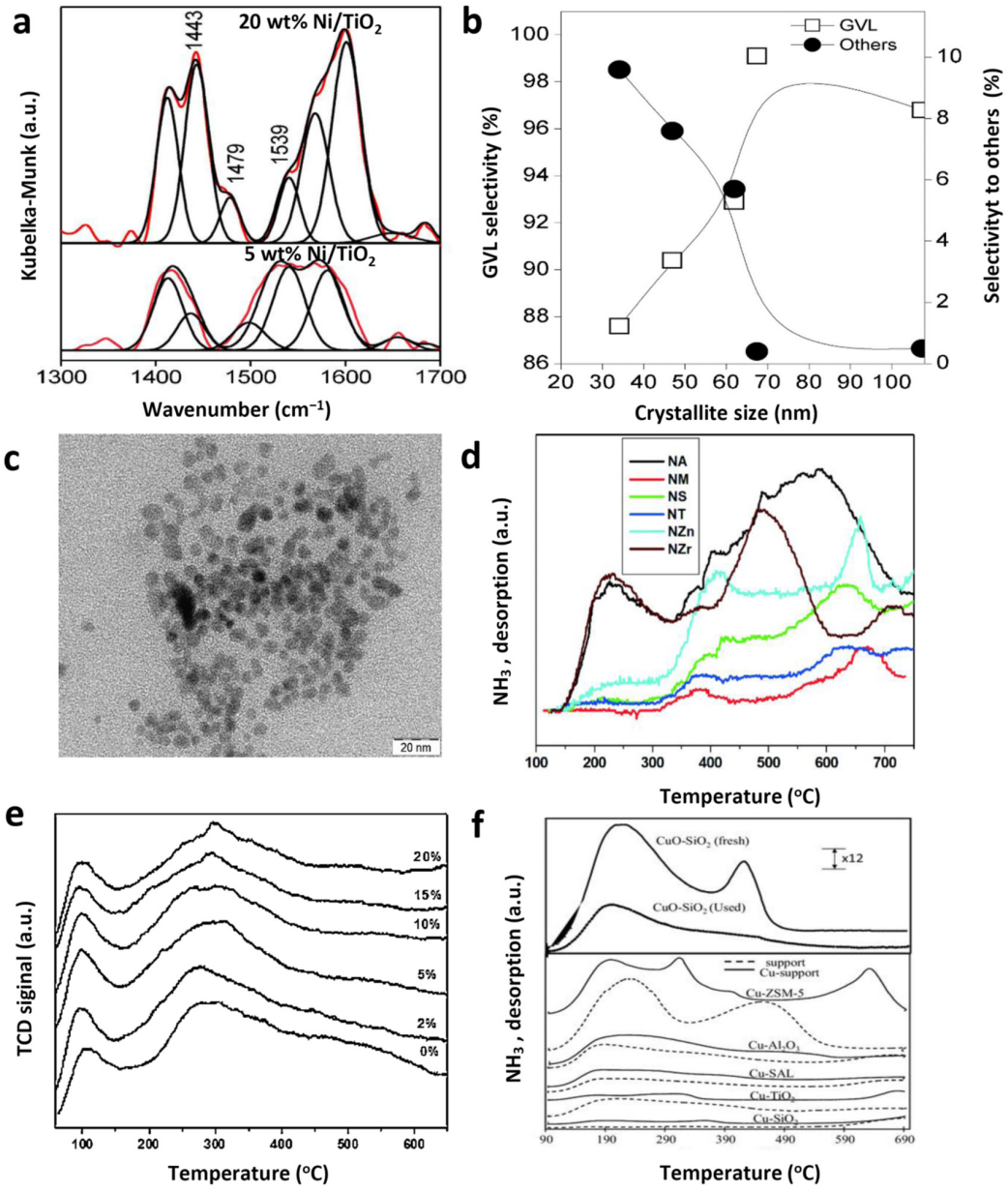

Figure 2. (**a**) Pyridine adsorbed DRIFT spectra of Ni/TiO_2 catalysts. (**b**) Products' selectivity versus the crystallite size of Ni/TiO_2 catalysts with different Ni loadings. Reaction conditions: 10 wt% LA in H_2O, 270 °C, GHSV = 3.247 mL g^{-1} s^{-1}. Reproduced with permission from Reference [52]. Copyright 2015, Elsevier Ltd. (**c**) TEM image of the Ni/SiO_2 catalyst. (**d**) NH_3-TPD profiles of the supported Ni catalysts. Reproduced with permission from Reference [53]. Copyright 2014, Royal Society of Chemistry. (**e**) NH_3-TPD profiles of various Cu/γ-Al_2O_3 catalysts. Reproduced with permission from Reference [54]. Copyright 2014, Elsevier Ltd. (**f**) NH_3-TPD profiles of different supports and Cu supported catalysts. Reproduced with permission from Reference [55]. Copyright 2017, Springer.

The dispersion and size of Cu nanoparticles, as well as their acidity, are also crucial for the hydrogenation of LA to GVL. Putrakumar et al. [54] reported the hydrogenation of LA to GVL under vapor-phase conditions over a series of Cu/γ–Al_2O_3 catalysts with different Cu loadings (2–20 wt.%) using a wet impregnation method at ambient pressure (Table 1, entries 11–15). A high metal dispersion of 55.7% and small Cu particle size of 1.86 nm were obtained for 5 wt% Cu/γ–Al_2O_3, which leads to excellent performance with 98% LA conversion and 87% selectivity toward GVL. Not only the Cu dispersion but also the catalyst acidity is affected by the Cu loading. The total acidity (including weak

and moderate acidity) increases with the increase of copper content from 2 to 5 wt% then decreases as the Cu loading is elevated to 20 wt.% (Figure 2e). The agglomeration of the Cu particles occurred at high loadings, which could be responsible for the decreased total acidity. According to the mechanism for the hydrogenation of LA to GVL, appropriate acidity is favorable. In order to further explore the potential effects of active site dispersion rather than total acidity on the performance of catalysts, a series of Cu-based catalysts with different supports, specifically Al_2O_3, SiO_2, TiO_2, ZSM-5 and SiO_2–Al_2O_3, were prepared and tested (Table 1, entries 16–20) [55]. It was found that 48% conversion of LA and 80% selectivity toward GVL were delivered over Cu/SiO_2 at 250 °C, meanwhile, relatively low LA conversion was observed over Cu/ZSM-5 (4%), Cu/SAL (6%) and Cu/TiO_2 (25%) with stronger acidity compared to Cu/SiO_2. Although Cu/SiO_2 exhibits the least acidity compared with the other catalysts (Figure 2f), a large number of Cu nanoparticles are highly dispersed in the supporting matrix, which could contribute to high hydrogenation activity. These results indicate that the dispersion of metal sites is crucial for GVL formation.

In recent years, cobalt catalysts have been widely used in the hydrogenation of LA to GVL. Compared with Cu– and Ni–based catalysts, Co–based catalysts are more efficient in terms of LA hydrogenation to GVL under milder conditions. Murugesan et al. [56] reported the template synthesis of Co–LA on commercial silica, and the subsequent pyrolysis resulted in the formation of cobalt nanoparticles (9–11 nm) (Figure 3a,b) as highly active (99% LA conversion) and selective (97% GVL selectivity) catalysts for the hydrogenation of LA to GVL under industrially viable conditions (30 bar H_2, 120 °C and 24 h). Novodárszki [57] prepared silica-supported Co catalysts with varied Co contents using a wet impregnation method. Solvent-free LA hydrogenation was studied over Co/SiO_2 by applying a fixed-bed microreactor. Consecutive hydrogenation/hydrogenolysis and dehydration proceeded over the catalyst with metallic Co and CoO_x sites. Co/SiO_2 catalyst yields 100% LA conversion and 99% GVL selectivity at 200 °C and 30 bar total pressure. Long et al. [58] prepared magnetic Co/Al_2O_3 catalysts with different molar ratios of Co/Al (1, 2, 3, 4 and 5), derived from hydrotalcite through a constant pH co-precipitation (Table 1, entries 21–25). XRD patterns show that there is a $CoAl_2O_4$ phase in the catalyst (Figure 3c). The $4Co/Al_2O_3$ exhibits the highest catalytic activity (100% conversion) with a low catalyst loading (1.5% LA) and a short duration (3 h) under mild conditions. No apparent relationship was found between the BET surface area/total acid sites and the catalytic properties of Co/Al_2O_3. However, relative to the surface Co/Al ratio, there was a good correlation between Co content and catalytic performance. In fact, the specific composition of $4Co/Al_2O_3$ can fully expose active Co species, which is crucial for achieving high efficiency in LA hydrogenation.

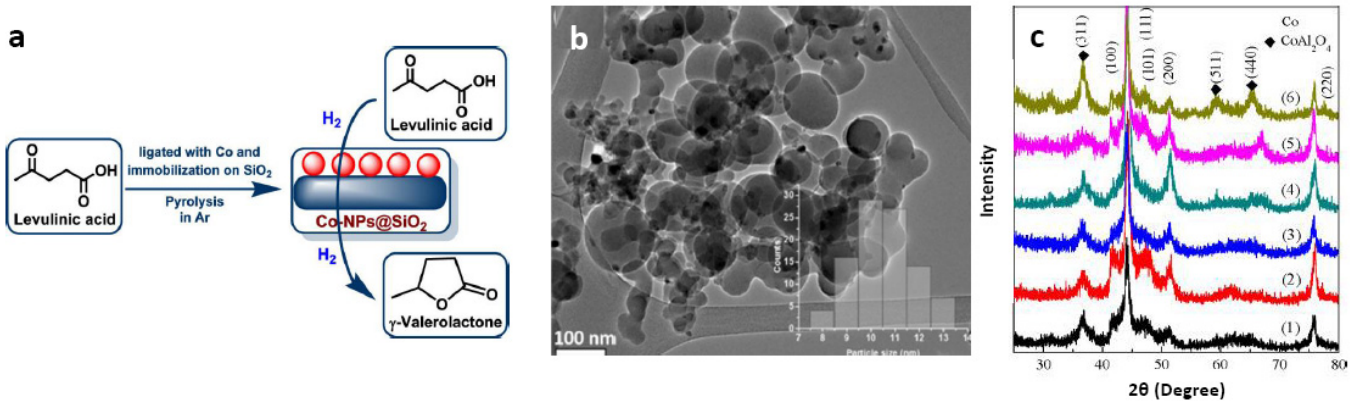

Figure 3. (**a**) Valorization of LA for the preparation of cobalt-based nanocatalysts and GVL. (**b**) TEM image of Co–LA@SiO_2–800. Reproduced with permission from Reference [56]. Copyright 2019, American Chemical Society. (**c**) XRD patterns of samples reduced with H_2 including (1) $5Co/Al_2O_3$, (2) $4Co/Al_2O_3$, (3) $3Co/Al_2O_3$, (4) $2Co/Al_2O_3$, (5) $1Co/Al_2O_3$ and (6) spent $4Co/Al_2O_3$. Reproduced with permission from Reference [58]. Copyright 2015, Elsevier Ltd.

Table 1. Single non-precious metal catalysts for the hydrogenation of LA to GVL.

Entry	Catalyst	H Donor	Solvent	Catalyst Amount (mg)	Metal Loading (wt.%)	LA Amount (mol)	Temperature (°C)	Time (h)	H_2 Pressure (MPa)	LA Conversion (%)	GVL Selectivity (%)	References
1	5 wt.%Ni/TiO_2	H_2	H_2O	-	5	10 [a]	270	-	-	26	88	
2	10 wt.%Ni/TiO_2	H_2	H_2O	-	10	10 [a]	270	-	-	55	90	
3	15 wt.%Ni/TiO_2	H_2	H_2O	-	15	10 [a]	270	-	-	80	93	[52]
4	20 wt.%Ni/TiO_2	H_2	H_2O	-	20	10 [a]	270	-	-	100	99	
5	25 wt.%Ni/TiO_2	H_2	H_2O	-	25	10 [a]	270	-	-	92	97	
6	40%Ni/MgO	H_2	1,4-dioxane	100	40	0.0086	160	1	3	43	97.3	
7	40%Ni/$MgAl_{0.5}O_{1.75}$	H_2	1,4-dioxane	100	40	0.0086	160	1	3	83	93.4	
8	40%Ni/$MgAlO_{2.5}$	H_2	1,4-dioxane	100	40	0.0086	160	1	3	100	99.7	[30]
9	40%Ni/$MgAl_2O_4$	H_2	1,4-dioxane	100	40	0.0086	160	1	3	100	94.9	
10	40%Ni/Al_2O_3	H_2	1,4-dioxane	100	40	0.0086	160	1	3	22	95.6	
11	Cu/γ-Al_2O_3 [c]	H_2	H_2O	300	5	10 [a]	265	-		98	87	
12	Cu/γ-Al_2O_3 [c]	H_2	H_2O	300	2	10 [a]	265	-		82	76	
13	Cu/γ-Al_2O_3 [c]	H_2	H_2O	300	10	10 [a]	265	-		76	71	[54]
14	Cu/γ-Al_2O_3 [c]	H_2	H_2O	300	15	10 [a]	265	-		69	66	
15	Cu/γ-Al_2O_3 [c]	H_2	H_2O	300	20	10 [a]	265	-		41	56	
16	Cu/SiO_2	FA		1000	6	1 [b]	250	10 [d]	0.1	48	17	
17	Cu/TiO_2	FA		1000	6	1 [b]	250	10 [d]	0.1	8	55	[55]
18	Cu/ZSM-5	FA		1000	6	1 [b]	250	10 [d]	0.1	38	82	
19	Cu/Al_2O_3	FA		1000	6	1 [b]	250	10 [d]	0.1	24	15	
20	Cu/SAL	FA		1000	6	1 [b]	250	10 [d]	0.1	48	64	
21	1 Co/Al_2O_3	H_2	1,4-dioxane	33	54	0.02	180	3	5	43	99	
22	2 Co/Al_2O_3	H_2	1,4-dioxane	25	70	0.02	180	3	5	46	99	
23	3 Co/Al_2O_3	H_2	1,4-dioxane	23	78	0.02	180	3	5	43	99	[58]
24	4 Co/Al_2O_3	H_2	1,4-dioxane	22	82	0.02	180	3	5	100	99	
25	5 Co/Al_2O_3	H_2	1,4-dioxane	21	85	0.02	180	3	5	93	99	

[a] The number represents 10 wt.% LA in H_2O. [b] The number represents 1 mL h^{-1}. [c] An aqueous solution of 10 wt% LA was passed through the reactor at the weight hourly space velocity 0.169 h^{-1}. [d] Time-on-stream.

3.2. Bimetallic Catalyst

Bimetallic catalysts are greatly favored for LA hydrogenation, since catalytic activity can be improved to a large extent based on the tailored electronic structure. Both the reactivity and adsorption properties of bimetallic particles are superior to those of each metal separately. The metal composition, particle size and synergism are of great importance to the enhancement of the performance of bimetallic catalysts.

For the LA-to-GVL process, the catalytic activity of Ni is second only to that of noble metal catalysts (Ru, Pt and Ir), and Cu plays a unique role in inhibiting carbon deposition. Based on these merits, Iker et al. [59] designed Al_2O_3-supported Ni–Cu bimetallic catalysts using impregnation and sol-gel methods (Table 2, entries 1–5). The Ni–Cu bimetallic catalyst prepared by the sol-gel method converted LA conversion completely, and 96% GVL selectivity was obtained at an operating temperature of 250 °C and pressure hydrogen of 6.5 MPa. As for single Ni catalyst, a 91% yield of GVL was obtained at 2 h, whereas significant carbon deposition was detected on the catalyst surface. The single Cu catalyst delivered 66% GVL yield after 6 h, but showed a low carbon deposition. Comparatively, the Ni–Cu bimetallic catalyst shows a similar activity (92% GVL yield at 2 h) to that of Ni catalyst, as well as a low carbon deposition in agreement with Cu catalyst. The Ni–Cu synergism can be attributed to the high performance of the Ni–Cu bimetallic catalyst. Furthermore, the sol-gel-prepared catalyst delivers a higher specific activity as compared to the catalysts prepared using a wet impregnation procedure (Figure 4a). Hydrotalcite-derived Cu/Ni/Mg/Al catalysts with different Cu^{2+}/Ni^{2+} ratios (Table 2, entries 6–15) were developed for aqueous LA hydrogenation at 140 °C, equipped with 30 bar of H_2 for 3 h [20]. Only 15% of the LA was converted over Ni/Mg/Al catalyst, and an 82% selectivity toward GVL was obtained for Cu/Mg/Al catalyst. It is found that the LA conversion increased from 15 to 100% as the Cu content was elevated from 0 to 28 wt%, while the selectivity toward GVL increased from 82 to 100% with the increase of Ni content from 0 to 18 wt%. In addition, the Mg species also play a positive role, and the LA conversion over Cu/Mg/Al was elevated from 3 to 100%, in contrast to Cu/Al catalyst. The incorporation of

magnesium into the catalyst resulted in increased Lewis basic sites (detected by CO_2-TPD) which activated the C=O group of LA and thereby promoted the hydrogenation of LA into GVL under mild reaction conditions (Figure 4b). Therefore, the excellent activity and selectivity of Cu/Ni/Mg/Al in terms of LA hydrogenation can be attributed to the synergism between Cu, Ni and MgO.

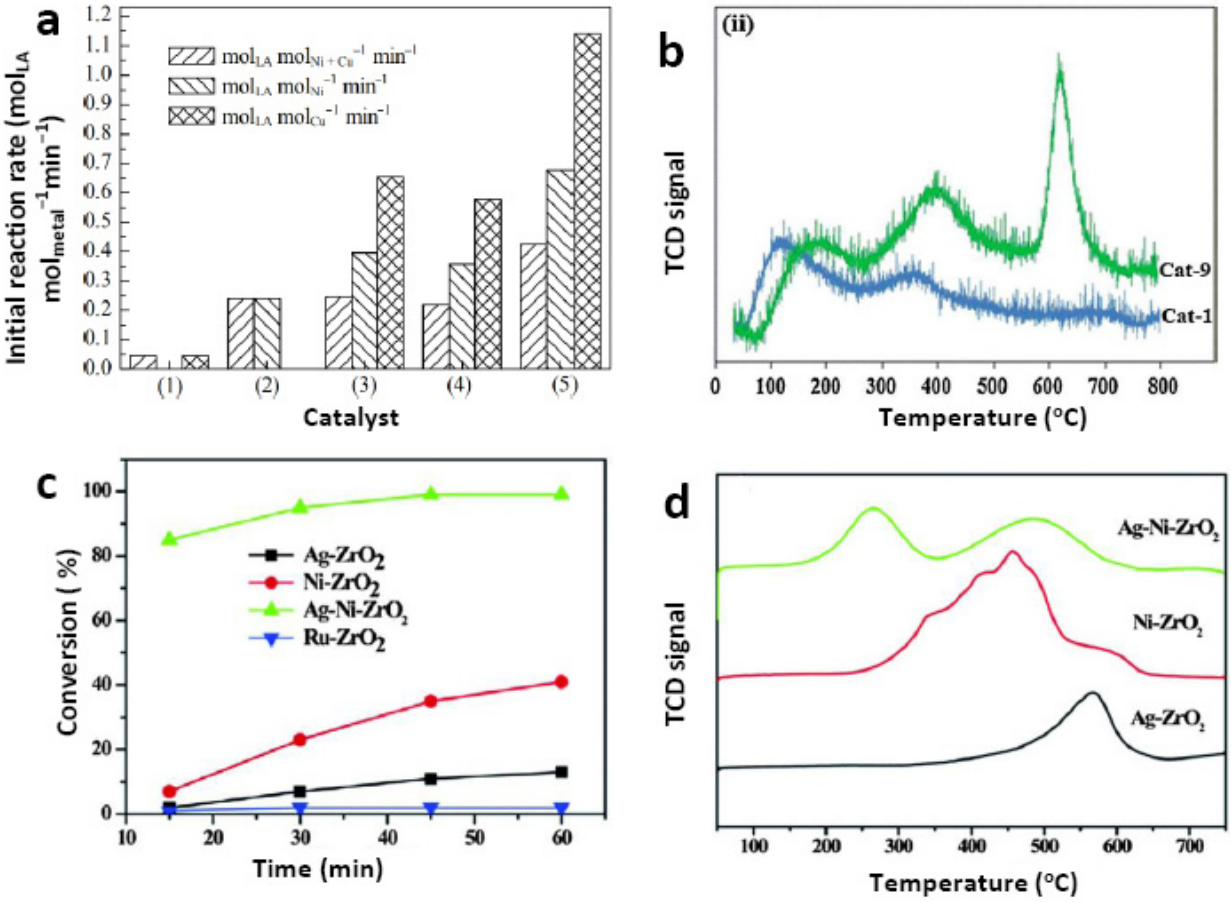

Figure 4. (**a**) Metal-normalized reaction rates over catalysts of (1) Cu/Al_2O_3 (WI), (2) Ni/Al_2O_3 (WI), (3) $Ni–Cu/Al_2O_3$ (WI), (4) $Ni–Cu/Al_2O_3$ (SG 300) and (5) $Ni–Cu/Al_2O_3$ (SG 450). Reproduced with permission from Reference [59]. Copyright 2014, Elsevier Ltd. (**b**) CO_2-TPD profiles of Cat-9 (Cu/Ni/Mg/Al with 0.75/0.5/1/1 molar ratio) and Cat-1 (Cu/Al with 1/1 molar ratio). Reproduced with permission from Reference [20]. Copyright, 2018 Elsevier Ltd. (**c**) FA decomposition profiles for Ag/ZrO_2, Ni/ZrO_2, $Ag–Ni/ZrO_2$ and Ru/ZrO_2. Reaction conditions: formic acid (43 mmol), water (90 mL), temperature (493 K), N_2 (1 atm) and catalyst (0.5 g). (**d**) H_2-TPR profiles of Ag/ZrO_2, $Ni/ZrO_2$and $Ag–Ni/ZrO_2$. Reproduced with permission from Reference [32]. Copyright 2014, Royal Society of Chemistry.

The synergism and size effect can improve the activity of bimetallic catalysts in a comprehensive way. For the LA-to-GVL process, Hengne et al. [32] developed $Ag–Ni/ZrO_2$ catalysts with varied Ag (Ni) contents (Table 2, entries 16–25). An excellent GVL yield (99%) was obtained over 10 wt%Ag-20 wt%Ni/ZrO_2 at 220 °C for 5 h. While only a 22 and 34% yield of GVL was delivered over 10 wt% Ag/ZrO_2 and 20 wt% Ni/ZrO_2, respectively (Figure 4c). The mixture of 10 wt% Ag/ZrO_2 and 20 wt% Ni/ZrO_2 was found to be laborious in improving the catalytic performance, and only a 41% GVL yield was achieved. The outstanding performance of the $Ag–Ni/ZrO_2$ catalyst can be attributed to the small size (−5 nm) and the synergism between Ag and Ni. The H_2-TPR profiles show two reduction peaks at low temperatures ascribed to the reduction of metal oxides due to the synergism between Ag and Ni (Figure 4d). In addition, the synergistic effect between

Ag and Ni facilitated the selective decomposition of formic acid into hydrogen, which provided enough hydrogen donors for LA hydrogenation to GVL.

Distinct from segregated metal species, the construction of bimetallic alloys as active sites has attracted much interest for LA hydrogenation recently. Al_2O_3-supported Cu–Co alloy catalysts (Figure 5a) with different Cu/Co weight ratios have been developed for the vapor phase hydrogenation of LA to GVL under ambient hydrogen pressure [60]. A Cu–Co/Al_2O_3 catalyst with a 2/3 Cu/Co weight ratio exhibits a superior activity and stability. It delivers a GVL productivity of 5.46 kg_{cat}^{-1} h^{-1} with a GVL selectivity of 99.1% at 250 °C for 24 h. Although GVL selectivity over 14Cu–6Co/Al_2O_3 catalyst exceeds 99%, Cu-rich Cu–Co/Al_2O_3 and Cu/Al_2O_3 catalysts show rapid deactivation in the initial period. In contrast to the Cu-rich catalysts, the stability of Co-rich Cu–Co/Al_2O_3 is outstanding in the initial 5 h (Figure 5b), and GVL was dominated over Co-rich catalysts, with trace acetone and 2-butanone. The reason for the above results is that the hydrogenation activity of Co-rich catalyst is higher than that of Cu-rich catalyst, so the Co-rich catalyst could inhibit the formation of carbon deposition. Saikiran et al. have developed silica nanosphere-supported CuNi bimetallic nanoalloys via solvothermal, impregnation and co-precipitation methods (Figure 6a), and evaluated their catalytic activity for the hydrogenation of LA. XRD investigations demonstrated that the Cu–Ni bimetallic nanoalloys were formed as synthesized by impregnation and co-precipitation methods, while only monometallic Cu(0) and Ni(0) nanoparticles can be detected as fabricated by the solvothermal method (Figure 6b). As listed in Table 2 (entries 26–31), the CuNi@SiO_2 catalyst developed using the impregnation method provided a 99.3% conversion of LA with a 96.8% selectivity toward GVL in 13 h at 120 °C [59]. This outstanding activity can be ascribed to the tailored electronic structure of the active sites with the introduction of another metal. Comparatively, the Ni was replaced by Co or Fe, and the LA conversion over CuCo@SiO_2 and CuFe@SiO_2 was found to be 42.8 and 23.6%, respectively (Table 2, entries 32,33). These results indicate that the synergism between Cu and Ni for CuNi@SiO_2 is more favorable for the hydrogenation of LA to GVL, as compared to that for CuCo@SiO_2 and CuFe@SiO_2. The reduction in temperature of Ni^{2+} declined in the presence of Cu. This implies that Cu has an unmatched promotion function in decreasing the reduction temperature of isolated Ni species in the Cu–Ni nanoalloy, thereby providing more reduced Ni sites.

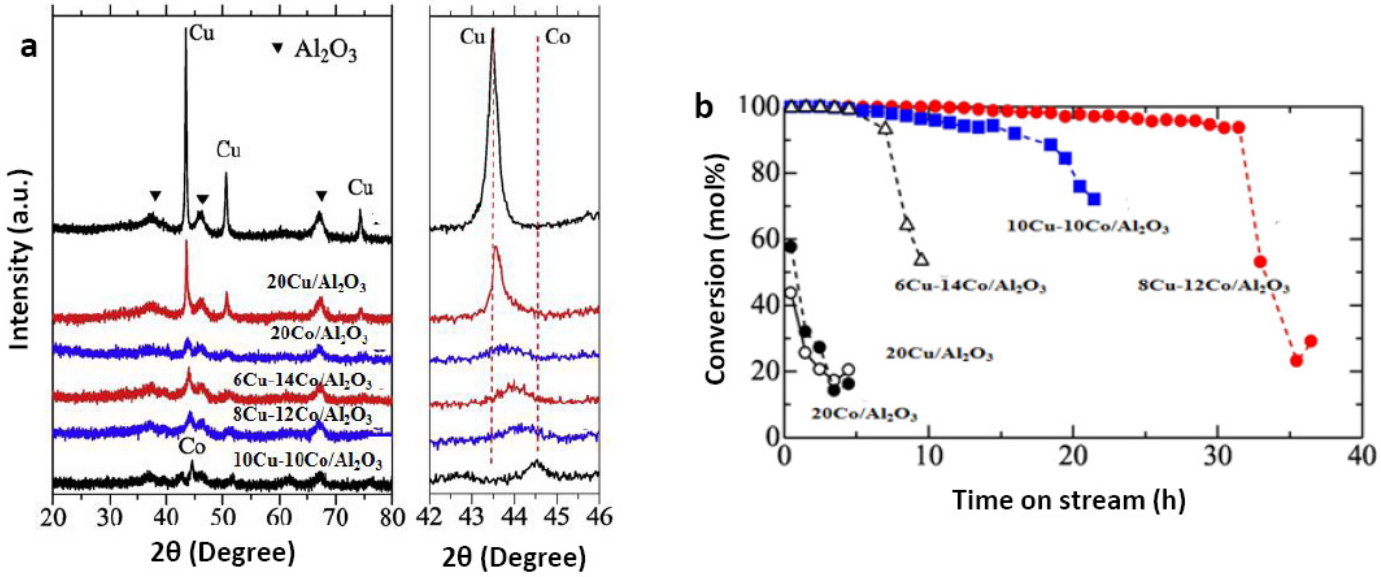

Figure 5. (**a**) XRD patterns and (**b**) change in the conversion in a long-run reaction for different catalysts. Reproduced with permission from Reference [60]. Copyright 2020, Elsevier Ltd.

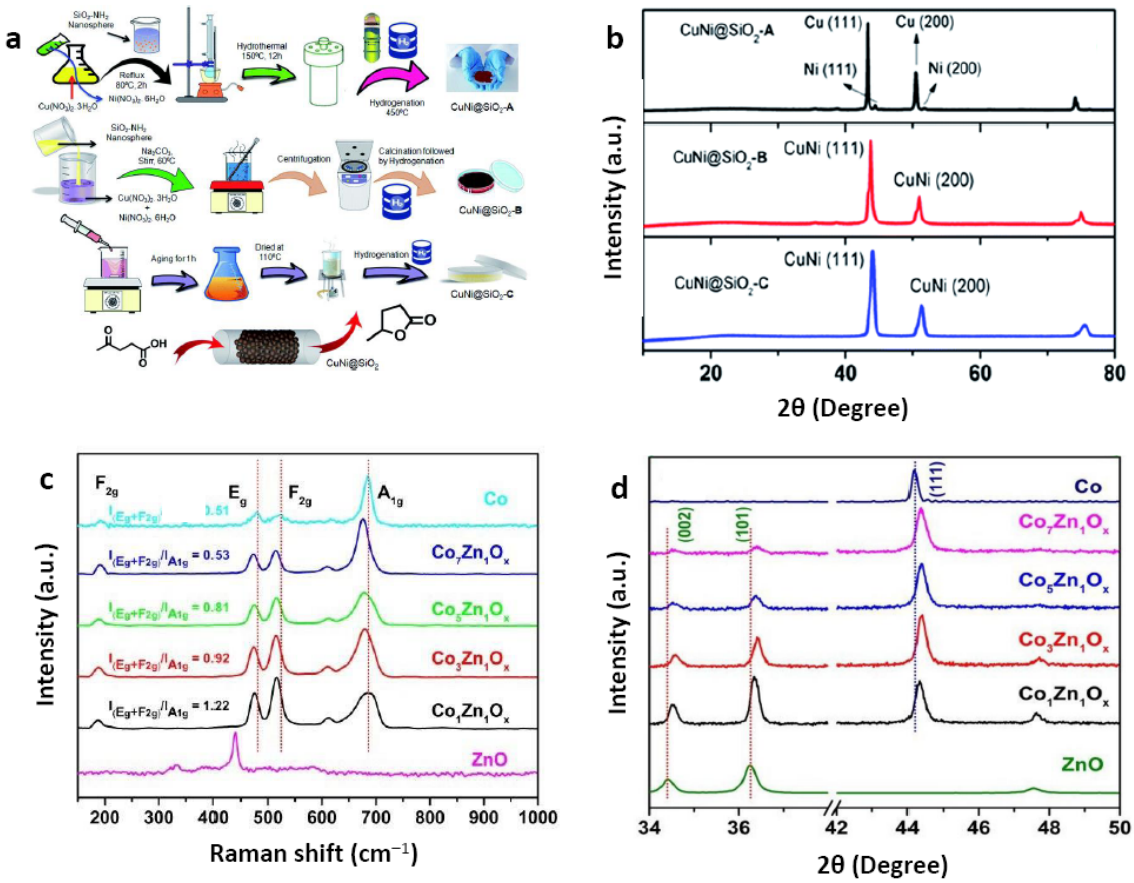

Figure 6. (**a**) Schematic illustration of the synthesis of Cu−Ni bimetallic nanoalloy catalysts using three different methods and their catalytic applications for LA hydrogenation to GVL. (**b**) Powder XRD spectra. Reproduced with permission from Reference [59]. Copyright 2014, Royal Society of Chemistry. (**c**) Raman spectra of catalysts. (**d**) XRD patterns of catalysts. Reproduced with permission from Reference [60]. Copyright 2020, Royal Society of Chemistry.

The strong interaction between different metal species is conducive to electron transport, which can greatly improve the activity of bimetallic catalysts. Co–Zn bimetallic alloy catalysts have been developed and screened with the goal of the hydrodeoxygenation (HDO) of biomass-derived oxygenates. A catalyst with a Co/Zn molar ratio of 5, denoted as $Co_5Zn_1O_x$, could enhance the catalytic activity significantly (Table 2, entries 34,35). Raman and XRD investigations show that the incorporation of Zn could stabilize Co^{2+} and denote electrons to Co species and oxygen vacancies, facilitating the capture of oxygen-containing groups **(**Figure 6c,d). It was found that 77% of GVL yield was achieved over $Co_5Zn_1O_x$, much higher than the 42% for Co catalyst. These results indicate that ZnO can improve the catalytic activity of Co catalysts towards the HDO of biomass-derived oxygenates.

3.3. Metal–Heteroatom (M-H) Active Sites

Besides the formation of bimetallic alloys in order to alter the electronic structure of active sites, the construction of heteroatom-doped metals has proven to be efficient in rendering an activity-dependent electronic structure by virtue of the enhanced interaction between metal sites and the doped supporting matrix. In this section, the active site structure and catalytic performance of heteroatom-doped non-precious metal catalysts (M-O and M-N) in terms of LA hydrogenation are summarized and discussed as shown in Tables 3 and 4.

Table 2. Bimetallic catalysts for the hydrogenation of LA to GVL.

Entry	Catalyst	H Donor	Solvent	Catalyst Amount (mg)	Metal Loading (wt.%)	LA Amount (mmol)	Temperature (°C)	Time (h)	H_2 Pressure (MPa)	LA Conversion (%)	GVL Selectivity (%)	References
1	Ni/Al_2O_3 (WI) [a]	H_2	H_2O	1000	36 (Ni)	200 [c]	250	6	6.5	100	91–92	[59]
2	Cu/Al_2O_3 (WI) [a]	H_2	H_2O	1000	30 (Cu)	200 [c]	250	6	6.5	75	66	
3	$Ni–Cu/Al_2O_3$ (WI) [a]	H_2	H_2O	1000	20 (Ni) 13 (Cu)	200 [c]	250	2	6.5	100	91–92	
4	$Ni–Cu/Al_2O_3$ (SG 300) [b]	H_2	H_2O	1000	13 (Ni) 9 (Cu)	200 [c]	250	2	6.5	100	96	
5	$Ni–Cu/Al_2O_3$ (SG 450) [b]	H_2	H_2O	1000	9 (Ni) 6 (Cu)	200 [c]	250	2	6.5	100	92	
6	Cu/Al	H_2	1,4-dioxane	100	70 (Cu)	4.3	140	3	3	76	58	[20]
7	Ni/Al	H_2	1,4-dioxane	100	54 (Ni)	4.3	140	3	3	8	8	
8	Mg/Al	H_2	1,4-dioxane	100	-	4.3	140	3	3	5	3	
9	Cu/Mg/Al	H_2	1,4-dioxane	100	41 (Cu)	4.3	140	3	3	100	82	
10	Ni/Mg/Al	H_2	1,4-dioxane	100	39 (Ni)	4.3	140	3	3	15	15	
11	Cu/Ni/Mg/Al	H_2	1,4-dioxane	100	30 (Cu) 28 (Ni)	4.3	140	3	3	100	100	
12	Cu/Ni/Mg/Al	H_2	1,4-dioxane	100	24 (Cu) 30 (Ni)	4.3	140	3	3	100	100	
13	Cu/Ni/Mg/Al	H_2	1,4-dioxane	100	18 (Cu) 32 (Ni)	4.3	140	3	3	80	78	
14	Cu/Ni/Mg/Al	H_2	1,4-dioxane	100	28 (Cu) 18 (Ni)	4.3	140	3	3	100	100	
15	Cu/Ni/Mg/Al	H_2	1,4-dioxane	100	33 (Cu) 10 (Ni)	4.3	140	3	3	100	85	
16	10% Ag/ZrO_2	FA	H_2O	500	10 (Ag)	43	220	5	-	22	22	[32]
17	20% Ni/ZrO_2	FA	H_2O	500	20 (Ni)	43	220	5	-	34	34	
18	10% Ag-20% Ni/ZrO_2	FA	H_2O	500	10 (Ag) 20 (Ni)	43	220	5	-	100	99	
19	10% Ag-20% Ni/ZrO_2	FA	H_2O	500	10 (Ag) 20 (Ni)	43	200	7	-	99	98	
20	10% Ag-20% Ni/ZrO_2	FA	H_2O	500	10 (Ag) 20 (Ni)	43	150	7	-	21	21	
21	10% Ag-20% Ni/ZrO_2	FA	H_2O	500	10 (Ag) 20 (Ni)	43	220	1	-	34	34	
22	5% Ag-20% Ni/ZrO_2	FA	H_2O	500	5 (Ag) 20 (Ni)	43	220	5	-	53	52	
23	10% Ag-10% Ni/ZrO_2	FA	H_2O	500	10 (Ag) 10 (Ni)	43	200	5	-	61	60	
24	10% Ag-20% Ni/ZrO_2	FA	H_2O	500	10 (Ag) 20 (Ni)	86	220	5	-	79	78	
25	10% Ag/ZrO_2 + 20% Ni/ZrO_2	FA	H_2O	500	10 (Ag) 20 (Ni)	43	220	5	-	41	41	
26	CuNi@SiO_2-A	H_2	2-PrOH [d]	65	-	2	120	13	4	68.9	75.3	[61]
27	CuNi@SiO_2-B	H_2	2-PrOH	65	22 (Cu) 11 (Ni)	2	120	13	4	99.3	96.8	
28	CuNi@SiO_2-C	H_2	2-PrOH	65	-	2	120	13	4	34.6	27.6	
29	Cu@SiO_2	H_2	2-PrOH	65	-	2	120	13	4	55.8	61.2	
30	Ni@SiO_2	H_2	2-PrOH	65	-	2	120	13	4	31.2	26.7	
31	Cu-SiO_2 + Ni-SiO_2	H_2	2-PrOH	65	-	2	120	13	4	75.6	65.3	
32	CuCo@SiO_2	H_2	2-PrOH	65	-	2	120	13	4	42.8	61.3	
33	CuFe@SiO_2	H_2	2-PrOH	65	-	2	120	13	4	23.6	52.3	
34	$Co_5Zn_1O_x$	H_2	MeOH [e]	20	19 (Co) 4 (Zn)	1	150	3	4	79	77	[62]
35	Co	H_2	MeOH	20	-	1	150	3	4	42	55	

[a] WI: prepared using the wet impregnation method. [b] SG: prepared using the sol-gel method. [c] The number represents 200 mL 5 wt% LA aqueous solution (98%, Aldrich). [d] 2-PrOH: isopropanol. [e] MeOH: methanol.

3.3.1. M-O Active Sites

LA hydrogenation to GVL with M-O active sites has been extensively explored, mainly originating from non-precious metal oxides and Zr-organic frameworks (Zr–MOFs). Metal ions often possess numerous valences and can tailor surface acidity/basicity, because of which the basic sites can activate carboxylic groups during hydrogenation reactions. Luque et al. [63] reported that supported Fe-oxide nanocatalysts are active for the microwave-assisted transformation of LA in FA. A simple and reproducible continuous flow method was used for the homogeneous deposition of Fe oxide nanoparticles (5–7 nm) on silica supports. The obtained Fe/Zr–SBA catalyst yields 30% LA conversion and 78% GVL selectivity, delivering a TOF value of 125 h^{-1}. The calcined hydrotalcite catalyst with a Mg/Al molar ratio of 3 yields 98% GVL selectivity, as LA is completely converted in FA until 10 h [64]. This is due to the presence of a large number of available active (basic)

sites, predominantly provided by OH^- groups, Mg–O pairs and O^{2-} ions on the catalyst surface. A Sn modified SBA-15 catalyst (SnO_2/SBA-15) was synthesized using a post-grafting method, and it was screened towards the hydrogenation of LA in 2-propanol [65]. The strong Lewis and Brønsted acidity originating from the well-dispersed Sn particles contributes to the formation of GVL. Excellent performance with 85.1% LA conversion and 95.2% GVL selectivity for SnO_2/SBA-15 can be attributed to the superior activity for hydrogen transfer and esterification. Kuwahara et al. developed a SBA-15-supported ZrO_2 catalyst, and 95% GVL yield was achieved over ZrO_2(10)/SBA-15 (10 wt% of ZrO_2) under mild reaction conditions (150 °C, 1.0 MPa Ar) [49]. It was found that the coordination of unsaturated Zr^{4+}-oxide is the dominant active site.

Lattice distortion leads to a change in the electronic properties at the interface of the catalyst species and the active center at the atomic scale. Wang et al. [66] developed an Mn_2CoO_x catalyst and discussed the effect of lattice-mismatch-induced structural distortion on catalytic C–H and C–O cleavage (Figure 7a). They proposed that MnCo–based oxides are crucial for the hydrogenation of LA to GVL using FA as the H-donor. It was found that the lattice planes of (110), (113) and (116) for $MnCoO_3$ undergo a structural distortion when increasing the Mn/Co molar ratio from 2/1 to 2/0.1 (Figure 7b). Such a lattice distortion induces an electronically coupled $MnCoO_3$ phase at the MnO_x–CoO_x interface, acting as the active site for the transfer hydrogenation. Lattice-distorted $MnCoO_3$ may decrease the energy barrier by facilitating H–H bond formation, favoring H_2 desorption for transfer hydrogenation reactions. More importantly, the decreased electronic binding energy at Co sites selectively promotes π–π interaction with the ketone group in LA. In this regard, Mn species can facilitate C–H splitting for H_2 generation with $MnCoO_3$ involved (Figure 7c).

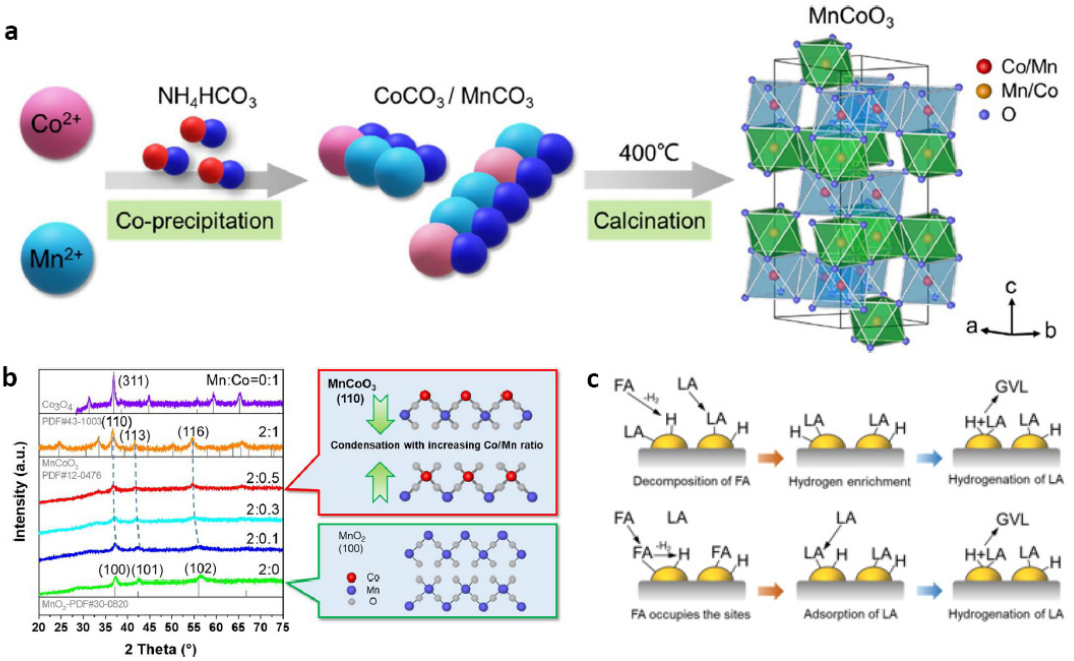

Figure 7. (**a**) Preparation process for MnCo oxide catalyst. (**b**) XRD patterns of MnCo oxide catalysts with different molar ratios. (**c**) Two proposed surface mechanisms over Mn_2CoO_x catalyst. Reproduced with permission from Reference [66]. Copyright 2020, Elsevier Ltd.

Metal–organic frameworks (MOF) have gained substantial attention recently, as their designable framework structures can be modularly built from transition-metal clusters and organic ligands. Besides their diverse structures, high surface area and large pore volume, the involved metal-oxygen moieties formed as O-containing struts can provide highly active sites for hydrogenation reactions. Zr-MOFs, such as acid-functionalized UiO-66 [67] and zirconium–cyanuric acid (Zr–CA) [68], have received a good deal of attention for

LA hydrogenation to GVL. Kuwahara et al. reported a CTH reaction for LA and its esters to produce GVL over sulfoacid-functionalized UiO-66 (UiO-66-SO_3H) (Figure 8a). With optimized SO_3H content, the UiO-66-SO_3H delivered an 85% yield of GVL (Table 3, entry 1), which far outperforms that over bulk ZrO_2 (6% GVL yield). The synergism between the Lewis basic $Zr_6O_4(OH)_4$ and Brønsted acidic SO_3H may be responsible for the high catalytic activity. The adjacent acid–base sites were confined in a nanospace, which catalyzed the CTH reaction of LA and its esters and facilitated successive intramolecular dealcoholization to afford GVL, respectively (Figure 8b). Xue et al. [68] developed a porous Zr–CA coordination polymer, that has proven to be efficient in the transfer hydrogenation reaction to produce GVL. They also proposed a reasonable reaction mechanism, suggesting that the acidic and basic sites on Zr–CA led to the dissociation of isopropyl alcohol to alkoxide and hydrogen. Meanwhile, Zr^{4+} in Zr–CA activated the carbonyl group in LA and its esters (Figure 8c). The abundant acid and base sites provided by Zr–CA contribute to the 96.8% GVL yield obtained at 130 °C for 4 h. Alternatively, a water-born Zr-containing MOF, Zr–fumarate (ZrF), was synthesized instead of using organic solvents like N,N-dimethylformamide [69]. In all, 96% LA conversion and 98% GVL selectivity were achieved over ZrF at 200 °C within 2 h (Table 3, entries 2,3). The excellent performance of ZrF can be attributed to the joint effects of acidic and basic sites originating from Zr^{4+} and O^{2-}, which are beneficial for a CTH reaction.

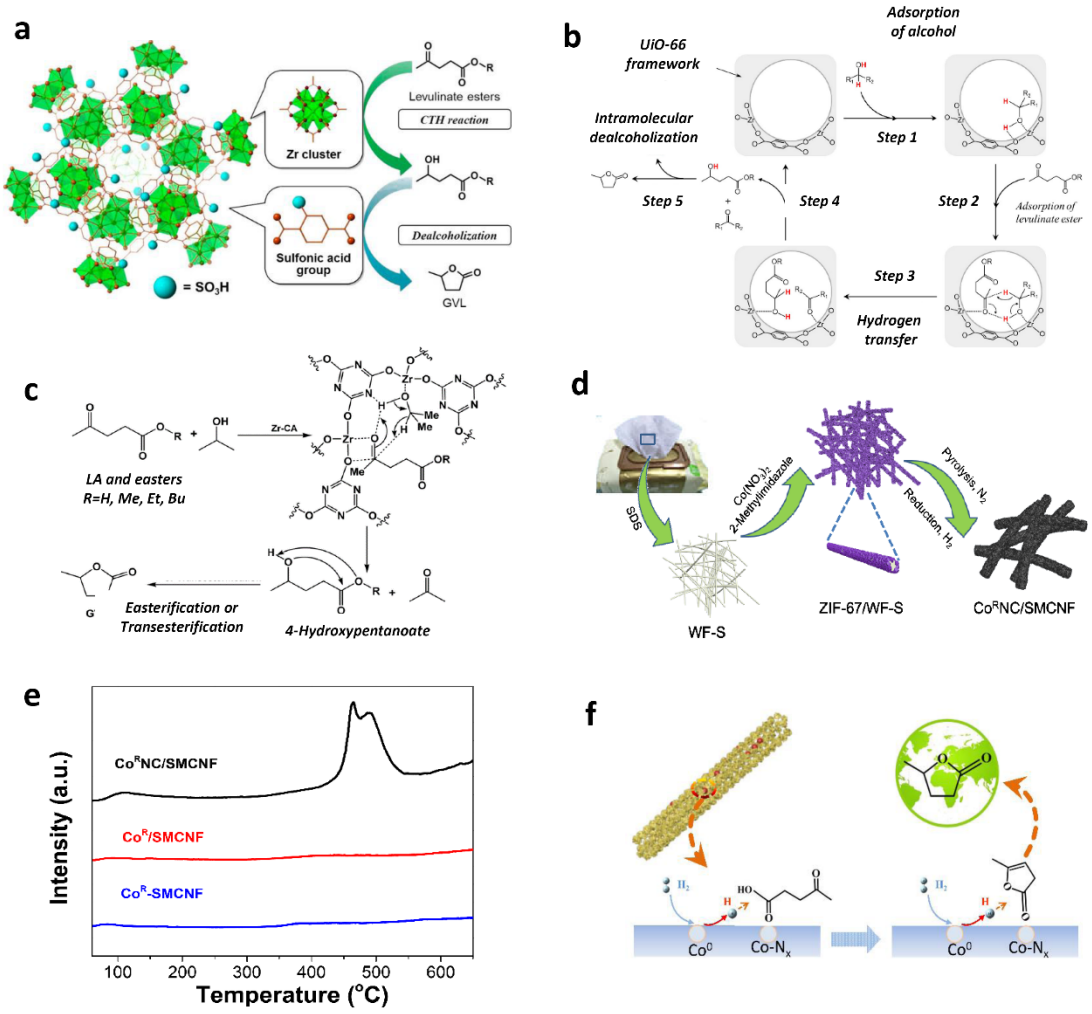

Figure 8. (**a**) Illustration of the structure of sulfonic acid-functionalized UiO-66 and the reaction pathway for the catalytic transfer hydrogenation (CTH) of LA or levulinate esters to produce GVL. (**b**) A possible reaction mechanism for CTH process of LA or levulinate esters to produce GVL over

UiO-66-S_x catalyst. Reproduced with permission from Reference [67]. Copyright 2017, American Chemical Society. (**c**) A plausible reaction mechanism for the CTH reaction of LA and its esters into GVL catalyzed by Zr–CA. Reproduced with permission from Reference [68]. Copyright 2016, Royal Society of Chemistry. (**d**) Schematic illustration of the synthesis process for Co^RNC/SMCNF. (**e**) CO_2 temperature-programmed desorption (CO_2-TPD) profiles of Co^RNC/SMCNF, Co^R/SMCNF and CoR–SMCNF. (**f**) Mechanistic model for the hydrogenation of LA to GVL over Co^RNC/SMCNF catalyst. Reproduced with permission from Reference [70]. Copyright 2020, Elsevier Ltd.

3.3.2. M-N Active Sites

The electronic structure of active sites can greatly be tailored via N-functionalization [71]. The pyrolysis of N–containing MOFs is an effective strategy for N-doping. In addition, unique morphology and abundant pores can be created upon MOFs that are pyrolyzed. Gong et al. [34] reported that Co-900 with Co–N_x active sites is highly active in the selective hydrogenation of various biomass-derived organic compounds, and 83% LA conversion and 96% GVL selectivity were observed under 2 MPa H_2 at 25 °C for 24 h (Table 3, entry 4). Comparatively, Co–N_x free Co nanoparticle (NP) catalysts prove to be less active, delivering the LA conversion lower than 20% (Table 3, entries 5–7). These results demonstrate that Co–N_x is responsible for enhanced hydrogenation performance. Shao et al. [71] designed evenly dispersed Co NPs in N-doped mesoporous carbon nanofibers (MCNF) as efficient catalysts for aqueous LA hydrogenation. An N-rich Co zeolitic imidazolate framework (ZIF-67) was anchored on the sodium dodecyl sulfate-modified wipe fiber (WF-S) to increase the dispersion of active site precursor, and Co NPs were uniformly embedded in N-doped MCNF (Co^RNC/SMCNF) after the solid-state conversion of precursor via a pyrolysis–reduction strategy (Figure 8d). Benefiting from the well-dispersed Co NPs and the dual metallic Co with Co–N_x, Co^RNC/SMCNF catalyst showed brilliant catalytic activity, delivering 99.5% LA conversion, 99% GVL selectivity and a high TOF value (206 h^{-1}). Comparatively, both N-free Co^R-SMCNF and Co^R/SMCNF displayed inferior catalytic performance (26 and 22% of GVL yield, respectively) toward aqueous LA hydrogenation (Table 3, entries 8–10). These results demonstrate that the Co and N sites are essential, and that the interaction between Co^0 and Co–N_x in Co^RNC/SMCNF is responsible for the high catalytic performance. Furthermore, the N species served as the basic sites to enhance the surface basicity, thus promoting the LA adsorption and consequently accelerating the hydrogenation reaction (Figure 8e,f). Later, they reported a new Co catalyst with a tailored Co NP/Co SA ratio in a hollow carbon sphere. It was found that such a yolk–shell-structured Co catalyst with equivalent nanoparticles and sing-atoms is highly active towards aqueous LA hydrogenation. It was demonstrated that the superior activity is attributed to the synergism of Co nanoparticles and single-atoms. Li et al. [33] reported a series of Co catalysts prepared by the encapsulation of Co NPs into N-doped carbons at different carbonization temperatures (Table 3, entries 11–17). It was found that Co@NC-800 could convert LA completely to GVL at 2 MPa H_2 and 220 °C for 5 h. To distinguish the role of metallic Co and Co–N_x, a poisoning test was performed in the presence of KSCN, since SCN^- shows a strong association with metallic Co. It was found that the GVL yield over Co@NC-800 was significantly decreased from 100 to 17.2% after KSCN was introduced, indicative of the main active site of metallic Co. They also found that 16 and 72% of LA was converted over Co@C-800 and Co@N-800, respectively. Thorough investigation revealed that Co@N-800 had more metallic Co species, suggesting that N-functionalization facilitated the $Co^{\delta+}$ reduction in situ.

3.4. Heterostructural Catalysts

Heterostructure widely exists in composites, constructed from different components that are tightly connected to form an interface. Owing to the strong interfacial interaction, defects including vacancy, dislocation, boundary and/or crack are often produced, and these can significantly alter the electronic structure of the interfacial active sites. The

synergy of different active sites is crucial in order to improve the catalytic performance of heterostructural catalysts, which may play complementary roles for GVL production.

A series of $CePO_4/CoP_2$ heterostructural catalysts with different Ce/Co molar ratios were developed for LA hydrogenation to GVL (Table 4, entries 1–5). The $(CePO_4)_{0.16}/Co_2P$ yielded 97.1% LA conversion and 98.2% GVL selectivity at 90 °C and 4 MPa H_2 for 1.5 h and an attractive TOF value of 0.61 s^{-1}. The $(CePO_4)_{0.16}/Co_2P$ is superior to $CePO_4$ and CoP_2 and comparable to precious metal catalysts in terms of activity. H_2-TPD investigation revealed that three typical $(CePO_4)_m/Co_2P$ catalysts (m = 0.08, 0.16 and 0.34) showed obvious H-desorption peaks below 100 °C, similar to the peak that appeared on pure $CePO_4$ (Figure 9a), indicating that $CePO_4$ was the key component in the activation of hydrogen. In view of the temperature range for the NH_3-desorption peak, the Co_2P surface was mostly composed of moderate and strongly acidic sites, and $CePO_4$ surface was dominated by weak acid sites (Figure 9b). The active sites on catalysts prepared are mostly present as L-acid site, especially on Co_2P (Figure 9c). In this regard, $CePO_4$ was the key component in the activation of hydrogen while Co2P with strong Lewis acidity facilitated the selective hydrogenation of LA to GVL [42].

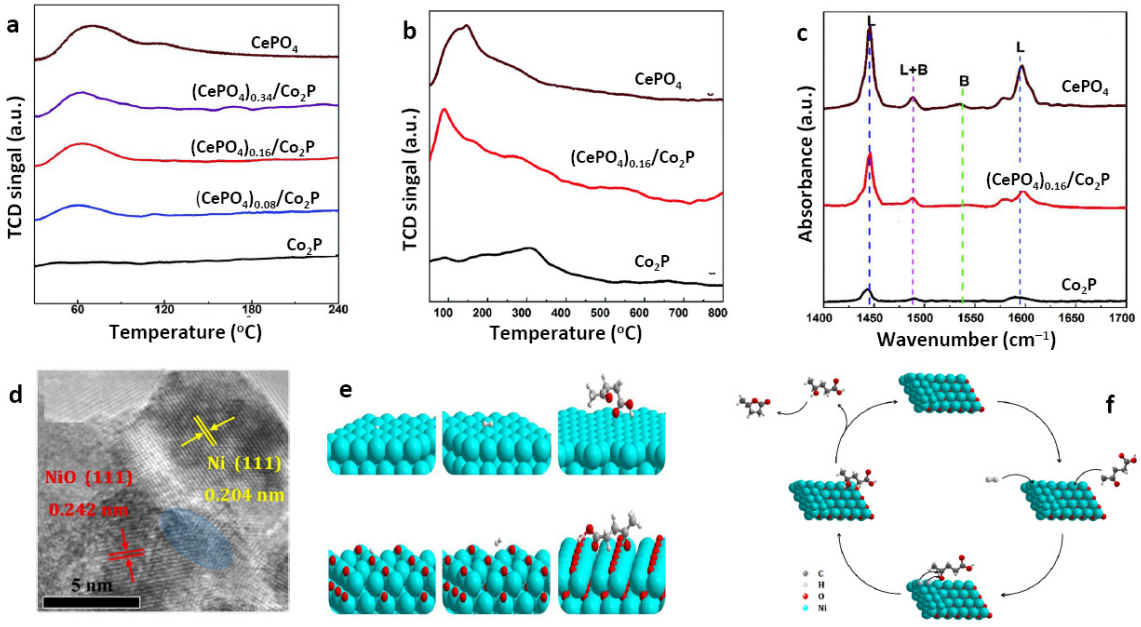

Figure 9. (**a**) H_2-TPD profiles of catalysts. (**b**) NH_3-TPD profiles of catalysts. (**c**) Pyridine (adsorbed) FT-IR spectra of catalysts (L: Lewis acid feature, B: Brønsted acid nature). Reproduced with permission from Reference [42]. Copyright 2013, Royal Society of Chemistry. (**d**) HRTEM image of NiO-523. (**e**) Structure models for H, H_2 and LA adsorption on Ni (111) and NiO (111). (**f**) Proposed mechanism for the hydrogenation of LA to GVL on Ni/NiO. Reproduced with permission from Reference [36]. Copyright 2017, Elsevier Ltd.

Ni/NiO catalyst was developed by 0NiO into metallic Ni in hydrogen at 200–300 °C [35]. High-resolution transmission electron microscopy (TEM) images show the existence of Ni/NiO heterojunctions in the NiO-523 catalyst (Figure 9d). The Ni/NiO catalyst shows a mass activity of 14.1 mmol GVL g^{-1} h^{-1} at 120 °C, which is 10–18 times higher than that of metallic Ni and NiO (Table 4, entries 6–12). Such high activity correlates with the formation of Ni/NiO heterojunctions. It reveals that LA was preferentially adsorbed on NiO, while H_2 was adsorbed on metallic Ni and then dissociated to produce atomic hydrogen, based on a cooperative Langmuir–Hinshelwood mechanism (Figure 9e,f).

Table 3. Non-precious metal–heteroatom catalysts for the hydrogenation of LA to GVL.

Entry	Catalyst	H Donor	Solvent	Catalyst Amount (g)	LA Loading (mmol)	Temperature (°C)	Time(h)	H_2 Pressure (MPa)	LA Conversion (%)	GVL Selectivity (%)	References
1	UiO-66-SO_3H	2-PrOH	2-PrOH	0.1	1	140	24	0.5 [a]	99	86	[67]
2	Zr-CA	2-PrOH	2-PrOH	0.2	1	130	4		100	97	[68]
3	ZrF	2-PrOH	H_2O	0.1	0.5	200	2	1 [b]	96	98	[69]
4	Co-900	H_2	H_2O	0.02	1	25	24	2	83	96	
5	Co-440	H_2	H_2O	0.02	1	60	6	2	14	97	[34]
6	Co-900-B	H_2	H_2O	0.02	1	60	6	2	15	97	
7	Co/AC	H_2	H_2O	0.02	1	60	6	2	2	95	
8	Co^RNC/SMCNF	H_2	H_2O	0.065	2	180	4	4.5	100	99	
9	Co^R-SMCNF	H_2	H_2O	0.065	2	180	2	4.5	59	44	[72]
10	Co^R/SMCNF	H_2	H_2O	0.065	2	180	2	4.5	47	47	
11	Co@NC-800	H_2	H_2O	0.1	8.6	220	5	2	100	100	
12	Co@NC-600	H_2	H_2O	0.1	8.6	220	5	2	11	83	
13	Co@NC-700	H_2	H_2O	0.1	8.6	220	5	2	96	98	
14	Co@NC-900	H_2	H_2O	0.1	8.6	220	5	2	93	99	[33]
15	Co@N-800	H_2	H_2O	0.1	8.6	220	5	2	45	95	
16	Co@C-800	H_2	H_2O	0.1	8.6	220	5	2	16	64	
17	Co/NC-800	H_2	H_2O	0.1	8.6	220	5	2	72	96	

[a] The pressure is supplied by Ar. [b] The pressure is supplied by N_2.

Table 4. Heterostructural catalysts for the hydrogenation of LA to GVL.

Entry	Catalyst	H Donor	Solvent	Catalyst Amount (g)	LA Loading (mmol)	Temperature (°C)	Time (h)	H_2 Pressure (MPa)	LA Conversion (%)	GVL Selectivity (%)	Mass Activity (mmol g^{-1} h^{-1})	References
1	$(CePO_4)_{0.16}/Co_2P$	H_2	H_2O	0.1	2	90	1.5	4	100	97	-	
2	Co_2P	H_2	H_2O	0.1	2	90	1.5	4	-	26	-	
3	$CePO_4$	H_2	H_2O	0.1	2	90	1.5	4	-	-	-	[42]
4	$(CePO_4)_{0.08}/Co_2P$	H_2	H_2O	0.1	2	90	1.5	4	-	72	-	
5	$(CePO_4)_{0.34}/Co_2P$	H_2	H_2O	0.1	2	90	1.5	4	-	61	-	
6	NiO-523	H_2	1,4-dioxane	0.2	10	120	24	2	100	100	14.1	
7	NiO	H_2	1,4-dioxane	0.2	10	120	-	2	-	100	0.8	[35]
8	Ni foil	H_2	1,4-dioxane	0.2	10	120	-	2	-	100	0.3	
9	NiO-473	H_2	1,4-dioxane	0.2	10	120	-	2	-	100	6.7	
10	NiO-573	H_2	1,4-dioxane	0.2	10	120	-	2	-	100	11.5	
11	NiO-673	H_2	1,4-dioxane	0.2	10	120	-	2	-	100	1.3	
12	NiO-773	H_2	1,4-dioxane	0.2	10	120	-	2	-	100	1.2	

4. Structure-Stability Relationship

Stability represents another key issue for non-precious metal-based hydrogenation catalysts, as the active site may be covered, "poisoned", aggregated or leached under acidic media and at a high temperature. The deposition of coke caused by support acidity not only reduces the catalytic activity, but it also leads to blockage as it is adhesive to the equipment and thereby may cause potential safety problems. Calcination and subsequent reduction treatments are effective for the regeneration of spent catalysts, whereas catalyst sintering occurs. Calcination is especially not suitable for carbon-supported catalysts, since the carbon will be removed. Nevertheless, metal sintering and leaching from the supporting matrix are irreversible, as non-precious metal-based catalysts are involved in aqueous LA hydrogenation. The metal species are inclined to accumulate at high temperatures, rendering aggregated nanoparticles with decreased dispersion which will ultimately erode the catalytic activity. The anchored metal species are highly susceptible to acidic media, and they leach out easily, leading to catalyst deactivation. In order to solve the problems above, the catalyst can be designed using the following strategies: (1) adjusting the acidity of catalysts, (2) designing the structure of special active sites, and (3) designing high-efficiency active sites in order to reduce the reaction temperature. In this section, we primarily focused on the active site structure–stability relationship for non-precious metal-based catalysts.

4.1. Strong Interaction between Active Site and Support

An increase to active site–support interaction has proven to be efficient in inhibiting metal leaching and sintering. Sultana et al. [55] developed a Cu–SiO_2 catalyst for the vapor-phase hydrogenation of LA with FA. The time-on-stream LA conversion and product selectivity vary little over the course of the whole reaction (Figure 10a). The H_2-TPR profile of Cu–SiO_2 shows a higher reduction temperature than that of other Cu catalysts (Figure 10b). This indicates a relatively stronger metal–support interaction which is responsible for the excellent stability of Cu–SiO_2. The stabilization of metal nanoparticles by N-coordination is also efficient in strengthening the active site–support interaction. Shao and his coworkers designed a new type of Co catalyst through the pyrolysis of ZIF-67/SDS (sodium dodecyl sulfate)-modified wipe fiber composite. The resulting Co nanoparticles are well dispersed and firmly embedded in the N-doped mesoporous carbon nanofibers [71]. Accordingly, the obtained $Co^{R}NC$/SMCNF delivered a higher reduction temperature than other analogues (Figure 10c), indicating a stronger interaction between Co nanoparticles and the carbon matrix. Such a strong metal–support interaction greatly inhibited the leaching of Co NPs from the N-doped mesoporous carbon nanofiber, and thus increased the reusability of $Co^{R}NC$/SMCNF (cycled nine times without notable loss of activity) (Figure 10d). The strong binding between metal nodes and O-containing struts presents another type of designed metal–support interaction. Xue et al. [68] synthesized a Zr–CA coordination polymer in which Zr was anchored to the framework of cyanuric acid. Screened as the catalyst for LA hydrogenation, the Zr-CA was cycled at least five times without a significant decrease in the catalytic activity (Figure 10e), probably because the metal leaching was effectively prohibited.

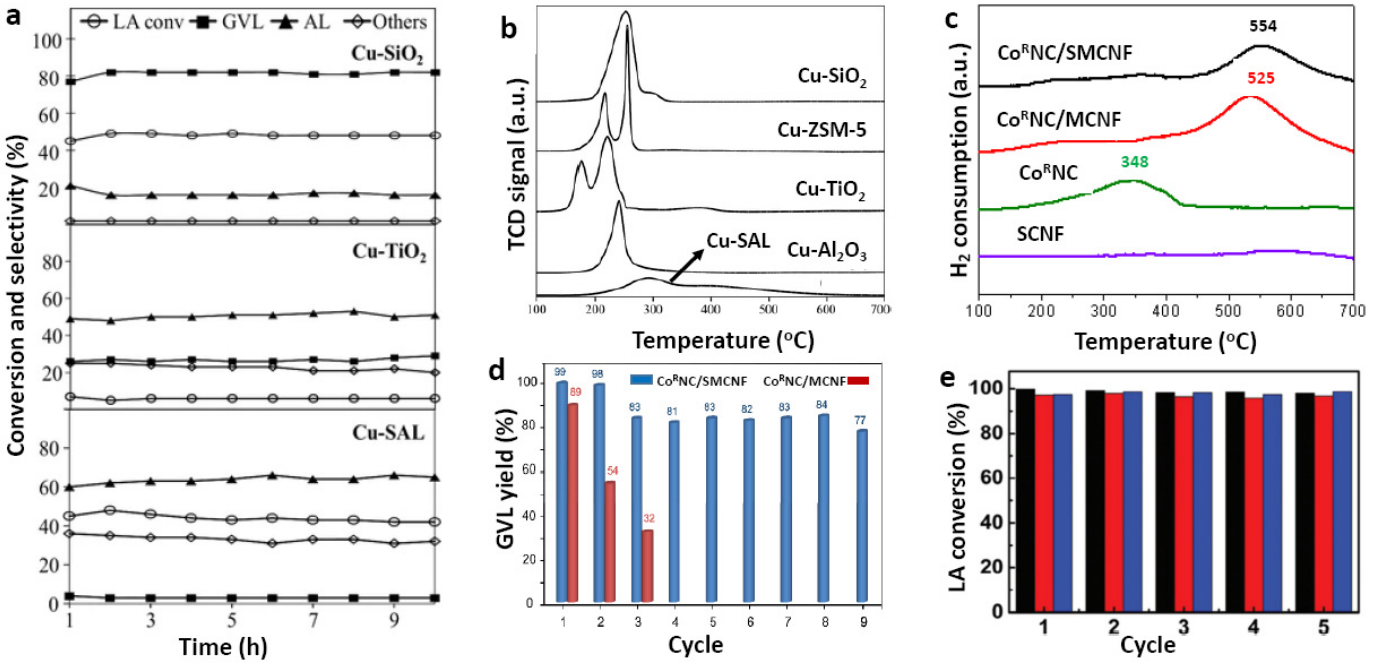

Figure 10. (**a**) Time-on-stream activity of catalysts. (**b**) H_2-TPR profiles of different supported copper catalysts. Reproduced with permission from Reference [55]. Copyright 2017, Springer. (**c**) H_2-TPR profiles of the SMCNF and Co-based catalysts. (**d**) Comparative stability investigation of $Co^{R}NC$/SMCNF and $Co^{R}NC$/MCNF. Reproduced with permission from Reference [72]. Copyright 2014, Elsevier Ltd. (**e**) The reusability of Zr–CA at 130 °C with a duration of 10 h. Reproduced with permission from Reference [68]. Copyright 2018, American Chemical Society.

4.2. Synergism of Bimetallic Catalysts

The introduction of another metal into non-precious metal catalysts to form bimetallic alloys is beneficial as it enhances the stability. Bimetallic catalysts are superior to single metal ones in terms of inhibiting carbon deposition and metal leaching. The ligand effect, stabilizing effect and/or electronic effect are responsible for the inherent stability of bimetallic catalysts. Iker and co-workers [59] found that the introduction of Cu into Ni-based catalyst reduced the carbon deposition significantly. In Pendem's study [61], the bimetallic Cu–Ni catalyst showed a stronger anti-oxidation ability in comparison with the monometallic Cu catalyst. The bimetallic CuNi@SiO_2 gave an 88.6% yield of GVL after exposure in air for 7 days, while Cu@SiO_2 delivered 6.8% GVL. The remarkably increased stability was attributed to the tailored electron property of active sites and their prevention from aggregation into large particles in the presence of another metal promoter. The cycling test indicates that CuNi@SiO_2 is stable and could be cycled 10 times without a drop in LA conversion and GVL yield. Ag was added to γ-Al_2O_3-supported Cu catalyst in order to prevent Cu leaching towards the LA hydrogenation to GVL [39]. The extent of Cu leaching distinctly changed with the catalyst component and the reaction condition. The leached Cu was as high as 176.5 ppm for CuO, but only 0.1 ppm for metallic Cu powder. This is because the formation of a soluble copper carboxylate complex as LA reacted with CuO accelerated the leaching of Cu species. As for $Cu_{0.8}Ag_{0.8}/Al_2O_3$, no metal leaching was observed to be conducting the reaction at 180 °C and 1.4 MPa of H_2 pressure. Therefore, Ag effectively eliminated Cu leaching from the $Cu_{0.8}Ag_{0.8}/Al_2O_3$ catalyst. The XPS spectra and H_2-TPR profiles revealed that Ag triggered the in situ reduction of Cu in $Cu_{0.8}Ag_{0.8}/Al_2O_3$ during the reaction (Figure 12a,b). Compared with the catalyst reduced by hydrogen, the particle size of in situ reduced $Cu_{0.8}Ag_{0.8}/Al_2O_3$ is smaller (Figure 12c,d). Figure 12e shows a possible mechanism for in situ reduction by hydrogen spillover and for the prevention of metal leaching as well as the reaction pathway. The outstanding stability (nine successive runs) is attributed to the strong interplay in the geometric and electronic effects between Cu and Ag.

4.3. Core–Shell Structure

The formation of core–shell structure in the catalyst can effectively prevent metal from leaching and sintering. In particular, in the core–shell configuration, the shell acts as an effective barrier to alleviate the erosion of the active sites. A Co/Al_2O_3 catalyst with a core–shell structure, as shown in Figure 11a, resulted in excellent stability, being reused five times without obvious performance degradation [58]. The leached Co ion was estimated to be 8 ppm, indicating that the Co/Al_2O_3 catalyst was stable under harsh conditions. The encapsulation of metal nanoparticles into the carbonaceous shell to form a core–shell structure is another strategy for improving catalyst stability. The carbon shell can reduce the metal species in situ by precisely adjusting the temperature and thereby alleviate the oxidation of the metal. As reported, a simple carbon coating was employed to encapsulate Co nanoparticles (NPs) into the carbon shell through the hydrothermal treatment of metal precursors with glucose [72]. During the carbon coating process, cobalt oxide was reduced to metallic Co and covered by thin carbon layers resulting a core–shell-structured Co@C catalyst (Figure 11b,c). These thin layers can not only prevent Co from leaching and sintering, but also prevent the deep oxidation of Co NPs. As expected, the Co@C catalyst was stable and could be reused five times for LA hydrogenation to GVL. Li and coworkers reported a facile and effective approach for synthesizing Co encapsulated in N-doped carbon matrix (Co@NC-800) using a combined coordination precipitation and pyrolysis strategy [33]. It was found that a high GVL yield of 80% remained after 10 runs, and no obvious metal loss was detected. Meanwhile, the carbon shell-free Co@N-800 exhibited poor stability and could only be cycled two times. The comparative study revealed that the carbon coating (Figure 11d) could improve the corrosion resistance of Co in acidic reaction media. Kong et al. [34] reported the use of N-doped carbon nanotubes to confine Co NPs (Co@NCNTs) (Figure 11e,f). In acid-resistant Co@NCNT-800, the Co NPs

are completely isolated within the bamboo-like NCNT, which could protect the Co NPs from agglomeration and leaching. The ICP-AES results showed that the leached Co was trace, and that Co@NCNT-800 could be cycled five times, outperforming most non-noble metal-based catalysts in aqueous media.

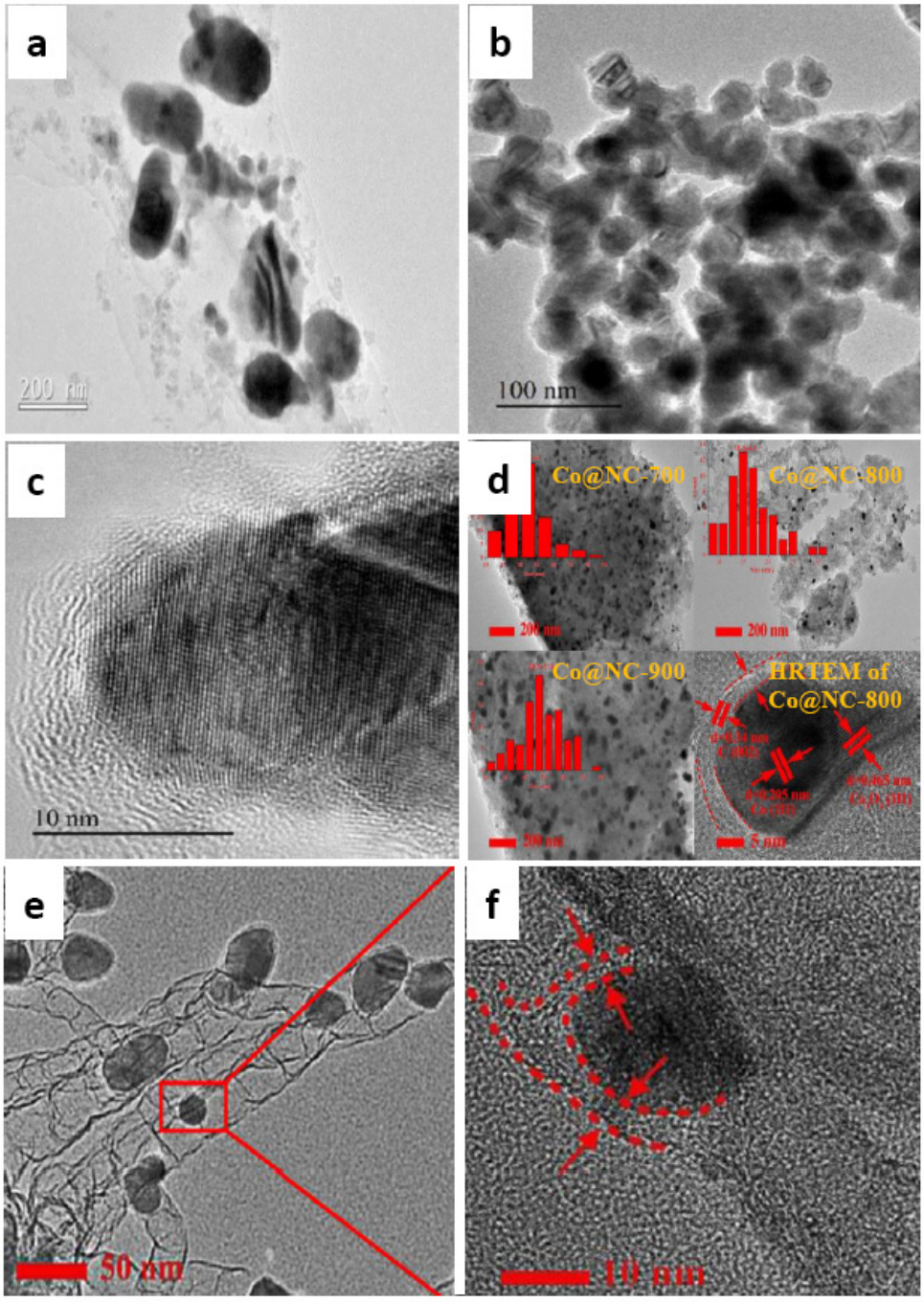

Figure 11. (**a**) TEM image of 4Co/γ-Al_2O_3. Reproduced with permission from Reference [58]. Copyright 2015, Elsevier Ltd. (**b**,**c**) TEM images of Co@C NPs. Reproduced with permission from Reference [72]. Copyright 2017, Elsevier Ltd. (**d**) The TEM images and the corresponding particle size distribution histograms for different Co@NC catalysts. Reproduced with permission from Reference [33]. Copyright 2020, Royal Society of Chemistry. (**e**,**f**) TEM images of Co@NCNT-800. Reproduced with permission from Reference [34]. Copyright 2021, Elsevier Ltd.

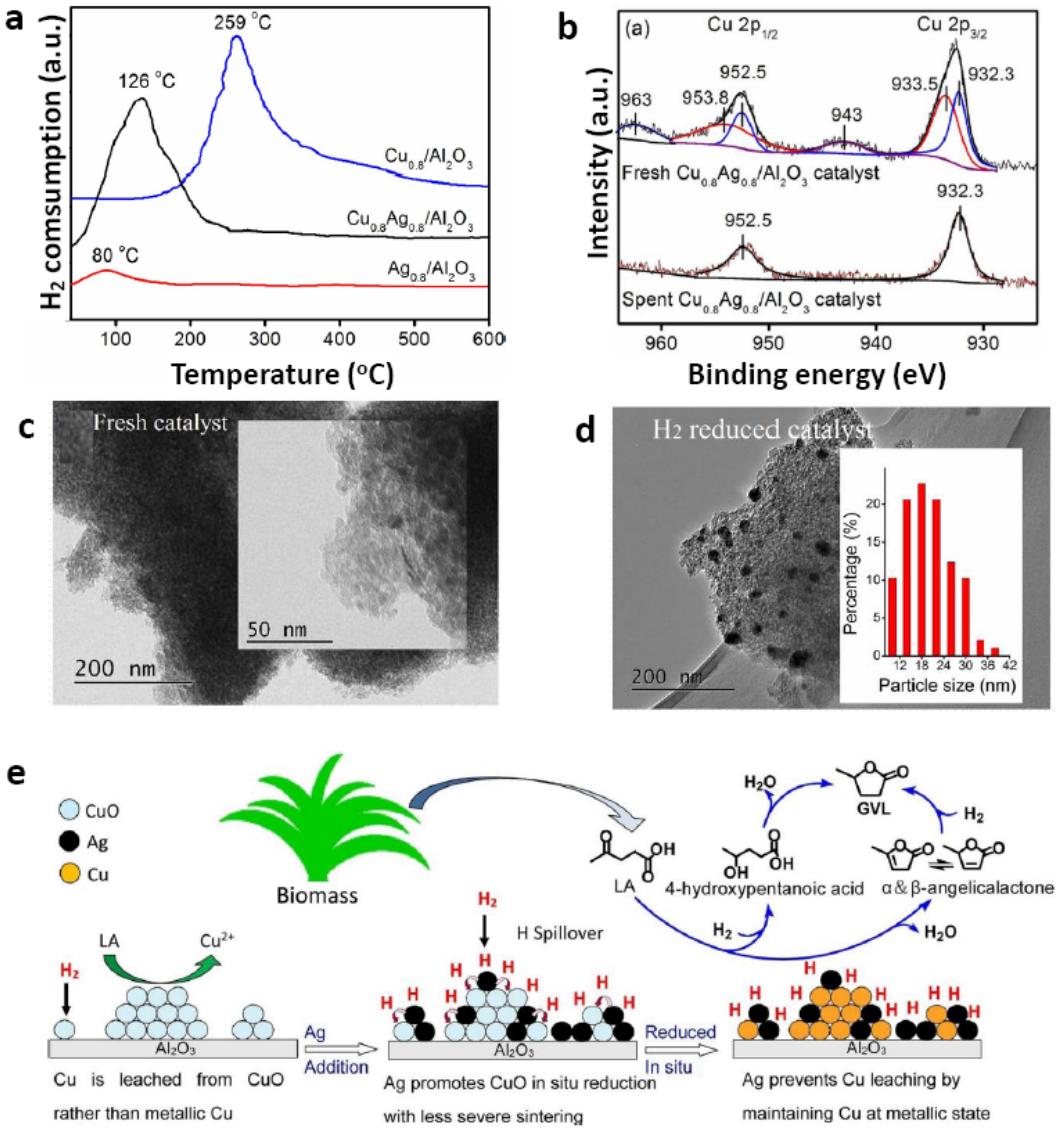

Figure 12. (**a**) TPR profiles of catalysts including $Cu_{0.8}/Al_2O_3$, $Cu_{0.8}Ag_{0.8}/Al_2O_3$ and $Ag_{0.8}/Al_2O_3$. (**b**) XPS spectra in the binding energy range of Cu 2p for fresh and spent $Cu_{0.8}Ag_{0.8}/Al_2O_3$. (**c**) TEM image of fresh $Cu_{0.8}Ag_{0.8}/Al_2O_3$. (**d**) TEM image of H_2-reduced $Cu_{0.8}Ag_{0.8}/Al_2O_3$ catalyst. (**e**) Schematic illustration of the proposed mechanism for in situ reduction, metal leaching prevention and reaction pathway. Reproduced with permission from Reference [39]. Copyright 2018, Elsevier Ltd.

4.4. Heterojunction

The formation of heterostructural nanoparticles can improve the stability of active components based on enhanced interaction at the heterojunction interface. The heterostructured Ni/NiO proved to be robust and could be recycled 10 times at 130 °C [35]. No significant leaching of Ni was detected (<0.5 ppm), attributed to the firm attachment of Ni at the Ni/NiO interface. The combination of $CePO_4$ with metal phosphide in the heterostructured structure can also improve the stability of catalysts, not only because of the strengthened interfacial interaction, but also because of their superior acid resistance over CeO and metal particles [42]. Slight fluctuations were observed for LA conversion and GVL yield as $(CePO_4)_m/Co_2P$ was involved in the continuous catalytic cycles, indicative of high stability. Although a small amount of Co was leached (3.0%) in the first run, and the leakage was gradually decreased in following cycles. The morphology, phase and surface

features of spent $(CePO_4)_{0.16}/Co_2P$ are similar to those of a fresh one, suggesting that the heterostructure was sufficiently robust to endure catalytic reuse in strongly acidic media.

5. Summary and Perspective

In this article, the reaction mechanism of LA hydrogenation to GVL with different hydrogen sources (H_2, FA and alcohol) is discussed first. However, due to the dependence on H_2 derived from fossil fuels, the large-scale production of GVL faces high production costs and potential safety risks. LA hydrogenation with FA and alcohol as internal hydrogen sources is considered to be the most promising for the synthesis of GVL. The FA/LA catalytic system is considered to be the most convenient way to synthesize GVL through a multi-step cascade reaction using cellulose carbohydrates as raw materials. Equimolar LA and FA can be produced by fructose dehydration via the 5-hydroxymethyl furfural intermediate. When alcohols are used as hydrogen donors, the CTH of LA belongs to the MPV reaction, which is a special way to realize a highly selective C=O hydrogenation in the presence of other functional groups. It is worth noting that ethanol is used as a hydrogen donor and carried out under mild conditions, making the process environmentally friendly and cost effective. In the following section, the structure–activity relationship was discussed in terms of single, bimetallic, heteroatom-doped and heterostructured non-precious metal-based active sites, referring to the particle size, dispersion and composition, etc. Finally, the structure–stability relationship was focused on, and it can be concluded that strong metal–support interaction and the core–shell structured configuration can prevent the leaching and sintering of active sites, while the synergism for heterostructural and bimetallic catalysts can enhance the interaction of different active components, all of which are beneficial for the lifespan of non-precious metal-based catalysts. Herein, some feasible suggestions are put forward as follows.

(1) High metal dispersion, tiny particles and optimum total acidity contribute significantly to LA hydrogenation. However, it is challenging to develop such non-precious metal-based catalysts because of their easy aggregation upon heat treatment. The characteristics of selected supports and catalyst preparation methods need to be considered comprehensively. This calls for new strategies to be explored in order to render preferable metal dispersion and loading. In addition, the non-precious metal single-atom catalysts with the highest metal dispersion may be promising for LA hydrogenation to GVL, though they are not referred to.

(2) The hydrogen source is crucial for LA hydrogenation to GVL. Compared with conventional hydrogenation routes, the management of liquid alcohols used in the CTH route is more convenient and promising. The CTH route via MPV reduction shows excellent selectivity to the carbonyl group in LA, avoiding the over-hydrogenated byproducts derived from GVL. Alcohol used as both solvent and internal hydrogen source decreases the process cost. LA hydrogenation to GVL via the CTH route can also overcome the drawbacks of the FA/LA catalytic system that require harsh temperatures or long reaction times and the higher requirements for metal active sites that are resistant to FA-poisoning. Therefore, it is highly desirable to develop high-performance non-precious metal-based catalysts with the goal of LA hydrogenation via the CTH route at a lower temperature, especially at room temperature.

(3) At present, M–N plays a positive role in the hydrogenation of LA to GVL in terms of activity and stability. However, the current M–N catalysts are limited to Co–N catalysts because of their facile synthesis from Co-containing MOFs. M–P catalysts can activate the carbonyl of LA and have been used in heterostructured catalysts which can be added into the library of the existing non-precious metal-based catalysts. In addition, M–S (metal–sulfur) catalysts may be feasible for LA hydrogenation, though they have not be investigated, and they are widely used in hydrodesulfurization, hydrodenitrogenation and aromatics hydrogenation reactions.

(4) Coking deposition, metal sintering and leaching are important factors in the deactivation of catalysts. The deactivation of catalyst caused by coke deposition is considered

to be reversible, and it can be reduced by a combination of calcination and reduction. However, repeated calcination may damage the structure of the catalyst. It is a promising strategy to design an active structure for the hydrogenation of LA to GVL at a mild temperature. New immobilization strategies, such as heteroatom doping and increasing the interaction between supports and active sites, are feasible and need to be further explored.

Author Contributions: Writing—review and editing, Y.Y. and Y.S.; visualization, X.L.; funding acquisition, Y.Y. All authors have read and agreed to the published version of the manuscript.

Funding: The National Key Research and Development Program of China (2018YFB1105100), the National Natural Science Foundation of China (51571211), and by funding from the Science Foundation of China University of Petroleum, Beijing (24620188JC005).

Institutional Review Board Statement: Not applicable.

Informed Consent Statement: Not applicable.

Data Availability Statement: Not applicable.

Acknowledgments: This work was financially supported by the National Key Research and Development Program of China (2018YFB1105100), the National Natural Science Foundation of China (51571211), and by funding from the Science Foundation of China University of Petroleum, Beijing (24620188JC005).

Conflicts of Interest: The authors declare no conflict of interest.

References

1. Hayes, D.J. An examination of biorefining processes, catalysts and challenges. *Catal. Today* **2009**, *145*, 138–151. [CrossRef]
2. Rose, M.; Palkovits, R. Cellulose-based sustainable polymers: State of the art and future trends, Macromol. *Rapid Comm.* **2011**, *32*, 1299–1311. [CrossRef] [PubMed]
3. Cherubini, F. The biorefinery concept: Using biomass instead of oil for producing energy and chemicals. *Energ. Convers. Manag.* **2010**, *51*, 1412–1421. [CrossRef]
4. Serrano-Ruiz, J.C.; Luque, R.; Sepulveda-Escribano, A. Transformations of biomass-derived platform molecules: From high added-value chemicals to fuels via aqueous-phase processing. *Chem. Soc. Rev.* **2011**, *40*, 5266–5281. [CrossRef]
5. Kan, T.; Strezov, V.; Evans, T.J. Lignocellulosic biomass pyrolysis: A review of product properties and effects of pyrolysis parameters. *Renew. Sust. Energ. Rev.* **2016**, *57*, 1126–1140. [CrossRef]
6. Yu, Z.H.; Lu, X.B.; Bai, H.; Xiong, J.; Feng, W.L.; Ji, N. Effects of solid acid supports on the bifunctional catalysis of levulinic acid to γ-valerolactone: Catalytic activity and stability. *Chem. Asian J.* **2020**, *15*, 1182–1201. [CrossRef]
7. Ármin, S.; Márk, M.; Dibó, G.; Mika, L.T. Microwave-assisted conversion of carbohydrates to levulinic acid: An essential step in biomass conversion. *Green Chem.* **2013**, *15*, 439–445.
8. Wright, W.R.H.; Palkovits, R. Development of heterogeneous catalysts for the conversion of levulinic acid to γ-valerolactone. *ChemSusChem* **2012**, *5*, 1657–1667. [CrossRef]
9. Horváth, I.T.; Mehdi, H.; Fábos, V.; Boda, L.; Mika, L.T. γ-Valerolactone-a sustainable liquid for energy and carbon-based chemicals. *Green Chem.* **2008**, *10*, 238–242. [CrossRef]
10. Manzer, L.E. Catalytic synthesis of α-methylene-γ-valerolactone: A biomass-derived acrylic monomer. *Appl. Catal. A Gen.* **2004**, *272*, 249–256. [CrossRef]
11. Du, X.L.; He, L.; Zhao, S.; Liu, Y.M.; Cao, Y. Hydrogen-independent reductive transformation of carbohydrate biomass into gamma-valerolactone and pyrrolidone derivatives with supported gold catalysts. *Angew. Chem. Int. Ed.* **2011**, *50*, 7815–7819. [CrossRef] [PubMed]
12. Bond, J.Q.; Alonso, D.M.; Wang, D.; West, R.M.; Dumesic, J.A. Integrated catalytic conversion of gamma-valerolactone to liquid alkenes for transportation fuels. *Science* **2010**, *327*, 1110–1114. [CrossRef] [PubMed]
13. Liu, Q.; Qiao, B.; Liu, F.; Zhang, L.; Su, Y.; Wang, A.; Zhang, T. Correction: Catalytic production of 1,4-pentanediol from furfural in a fixed-bed system under mild conditions. *Green Chem.* **2020**, *22*, 3532–3538. [CrossRef]
14. Al-Shaal, M.G.; Dzierbinski, A.; Palkovits, R. Solvent-free γ-valerolactone hydrogenation to 2-methyltetrahydrofuran catalysed by Ru/C: A reaction network analysis. *Green Chem.* **2014**, *16*, 1358–1364. [CrossRef]
15. Carine, C.; Marcello, M.; Rinaldo, P.; Ravasio, N.; Zaccheriaa, A.F. New generation biofuels: γ-valerolactone into valeric esters in one pot. *RSC Adv.* **2013**, *3*, 1302–1306.
16. Yan, K.; Lafleur, T.; Wu, X.; Chai, J.; Wu, G.; Xie, X. Cascade upgrading of γ-valerolactone to biofuels. *Chem. Commun.* **2015**, *51*, 6984–6987. [CrossRef]

17. Molleti, J.; Tiwari, M.S.; Yadav, G.D. Novel synthesis of Ru/OMS catalyst by solvent-free method: Selective hydrogenation of levulinic acid to γ-valerolactone in aqueous medium and kinetic modelling. *Chem. Eng. J.* **2018**, *334*, 2488–2499. [CrossRef]
18. Li, W.; Xie, J.; Lin, H.; Zhou, Q. Highly efficient hydrogenation of biomass-derived levulinic acid to γ-valerolactone catalyzed by iridium pincer complexes. *Green Chem.* **2012**, *14*, 2388–2390. [CrossRef]
19. Yan, K.; Lafleur, T.; Jarvis, C.; Wu, G. Clean and selective production of γ-valerolactone from biomass-derived levulinic acid catalyzed by recyclable Pd nanoparticle catalyst. *J. Clean. Prod.* **2014**, *72*, 230–232. [CrossRef]
20. Gupta, S.S.R.; Kantam, M.L. Selective hydrogenation of levulinic acid into γ-valerolactone over Cu/Ni hydrotalcite-derived catalyst. *Catal. Today* **2018**, *309*, 189–194. [CrossRef]
21. Liu, D.; Zhang, L.; Han, W.; Tang, M.; Zhou, L.; Zhang, Y.; Li, X.; Qin, Z.; Yang, H. One-step fabrication of Ni-embedded hierarchically-porous carbon microspheres for levulinic acid hydrogenation. *Chem. Eng. J.* **2019**, *369*, 386–393. [CrossRef]
22. Dutta, S.; Yu, I.K.; Tsang, D.C.; Ng, Y.H.; Ok, Y.S.; Sherwood, J.; Clark, J.H. Green synthesis of gamma-valerolactone (GVL) through hydrogenation of biomass-derived levulinic acid using non-noble metal catalysts: A critical review. *Chem. Eng. J.* **2019**, *372*, 992–1006. [CrossRef]
23. Chia, M.; Dumesic, J.A. Liquid-phase catalytic transfer hydrogenation and cyclization of levulinic acid and its esters to γ-valerolactone over metal oxide catalysts. *Chem. Commun.* **2011**, *47*, 12233–12235. [CrossRef]
24. Yu, Z.H.; Lu, X.B.; Xiong, J.; Ji, N. Transformation of levulinic acid to valeric biofuels: A review on heterogeneous bifunctional catalytic systems. *ChemSusChem* **2019**, *12*, 3915–3930. [CrossRef] [PubMed]
25. Upare, P.P.; Lee, J.; Hwang, Y.K.; Hwang, D.W.; Lee, J.; Halligudi, S.B.; Hwang, J.; Chang, J. Direct hydrocyclization of biomass-derived levulinic acid to 2-methyltetrahydrofuran over nanocomposite copper/silica catalysts. *ChemSusChem* **2011**, *4*, 1749–1752. [CrossRef] [PubMed]
26. Zhong, H.; Li, Q.; Liu, J.; Yao, G.; Wang, J.; Zeng, X.; Huo, Z.; Jin, F. New method for highly efficient conversion of biomass-derived levulinic acid to γ-valerolactone in water without precious metal catalysts. *ACS Sustain. Chem. Eng.* **2017**, *5*, 6517–6523. [CrossRef]
27. Grilc, M.; Likozar, B. Levulinic acid hydrodeoxygenation, decarboxylation and oligmerization over $NiMo/Al_2O_3$ catalyst to bio-based value-added chemicals: Modelling of mass transfer, thermodynamics and micro-kinetics. *Chem. Eng. J.* **2017**, *330*, 383–397. [CrossRef]
28. Kumar, V.V.; Naresh, G.; Sudhakar, M.; Anjaneyulu, C.; Bhargava, S.K.; Tardio, J.; Reddy, V.K.; Padmasri, A.H.; Venugopal, A. An investigation on the influence of support type for Ni catalyzed vapor phase hydrogenation of aqueous levulinic acid to γ-valerolactone. *RSC Adv.* **2016**, *6*, 9872–9879. [CrossRef]
29. Sudhakar, M.; Kumar, V.V.; Naresh, G.; Kantam, M.L.; Bhargava, S.K.; Venugopal, A. Vapor phase hydrogenation of aqueous levulinic acid over hydroxyapatite supported metal (M = Pd, Pt, Ru, Cu, Ni) catalysts. *Appl. Catal. B Environ.* **2016**, *180*, 113–120. [CrossRef]
30. Jiang, K.; Sheng, D.; Zhang, Z.; Fu, J.; Hou, Z.; Lu, X. Hydrogenation of levulinic acid to γ-valerolactone in dioxane over mixed $MgO–Al_2O_3$ supported Ni catalyst. *Catal. Today* **2016**, *274*, 55–59. [CrossRef]
31. Hengst, K.; Ligthart, D.M.; Doronkin, D.E.; Walter, K.M.; Kleist, W.; Hensen, E.J.M.; Grunwaldt, J. Continuous synthesis of γ-valerolactone in a trickle-bed reactor over supported nickel catalysts. *Ind. Eng. Chem. Res.* **2017**, *56*, 2680–2689. [CrossRef]
32. Hengne, A.M.; Malawadkar, A.V.; Biradar, N.S.; Rode, C.V. Surface synergism of an $Ag–Ni/ZrO_2$ nanocomposite for the catalytic transfer hydrogenation of bio-derived platform molecules. *RSC Adv.* **2014**, *4*, 9730–9736. [CrossRef]
33. Li, W.; Geng, W.; Liu, L.; Shang, Q.; Liu, L.; Kong, X. In situ-generated Co embedded in N-doped carbon hybrids as robust catalyst for the upgrading of levulinic acid in aqueous phase. *Sustain. Energy Fuels* **2020**, *4*, 2043–2054. [CrossRef]
34. Gong, W.; Lin, Y.; Chen, C.; Al-Mamun, M.; Lu, H.S.; Wang, G.; Zhang, H.; Zhao, H. Nitrogen-doped carbon nanotube confined $Co–N_x$ sites for selective hydrogenation of biomass-derived compounds. *Adv. Mater.* **2019**, *31*, 1808341. [CrossRef] [PubMed]
35. Song, S.; Yao, S.; Cao, J.; Guan, N.; Li, L. Heterostructured Ni/NiO composite as a robust catalyst for the hydrogenation of levulinic acid to γ-valerolactone. *Appl. Catal. B Environ.* **2017**, *217*, 115–124. [CrossRef]
36. Ye, L.; Han, Y.; Feng, J.; Lu, X. A review about GVL production from lignocellulose: Focusing on the full components utilization. *Ind. Crop. Prod.* **2020**, *144*, 112031–112047. [CrossRef]
37. Xu, Q.; Li, X.; Pan, T.; Yu, C.; Deng, J.; Guo, Q.; Fu, Y. Supported copper catalysts for highly efficient hydrogenation of biomass-derived levulinic acid and γ-valerolactone. *Green Chem.* **2015**, *4*, 2043–2054. [CrossRef]
38. Zhang, L.; Mao, J.; Li, S.; Zhou, J.; Jiang, C. Hydrogenation of levulinic acid into gamma-valerolactone over in situ reduced CuAg bimetallic catalyst: Strategy and mechanism of preventing Cu leaching. *Appl. Catal. B Environ.* **2010**, *232*, 1–10. [CrossRef]
39. Wang, J.; Jaenicke, S.; Chuah, G. Zirconium-beta zeolite as a robust catalyst for the transformation of levulinic acid to γ-valerolactone via meerwein–ponndorf–verley reduction. *RSC Adv.* **2014**, *4*, 13481–13489. [CrossRef]
40. Yang, Z.; Huang, Y.B.; Guo, Q.X.; Fu, Y. Ni catalyzed transfer hydrogenation of levulinate esters to γ-valerolactone at room temperature. *Chem Commun.* **2013**, *49*, 5328–5330. [CrossRef]
41. Abdelrahman, O.A.; Heyden, A.; Bond, J.Q. Analysis of kinetics and reaction pathways in the aqueous-phase hydrogenation of levulinic acid to form γ-valerolactone over Ru/C. *ACS Catal.* **2014**, *4*, 1171–1181. [CrossRef]
42. Feng, H.; Li, X.; Qian, H.; Zhang, Y.; Zhang, D.; Zhao, D.; Hong, S.G.; Zhang, N. Efficient and sustainable hydrogenation of levulinic-acid to gamma-valerolactone in aqueous solution over acid-resistant $CePO_4/Co_2P$ catalysts. *Green Chem.* **2019**, *21*, 1743–1756. [CrossRef]

43. Sun, D.; Takahashi, Y.; Yamada, Y.; Sato, S. Efficient formation of angelica lactones in a vapor-phase conversion of levulinic acid. *Appl. Catal. A Gen.* **2016**, *526*, 62–69. [CrossRef]
44. Yan, Z.; Lin, L.; Liu, S. Synthesis of γ-valerolactone by hydrogenation of biomass-derived levulinic acid over Ru/C catalyst. *Energy Fuel* **2009**, *23*, 3853–3858. [CrossRef]
45. Upare, P.P.; Lee, J.; Hwang, D.W.; Halligudi, S.B.; Hwang, Y.K.; Chang, J. Selective hydrogenation of levulinic acid to γ-valerolactone over carbon-supported noble metal catalysts. *J. Ind. Eng. Chem.* **2011**, *17*, 287–292. [CrossRef]
46. Mamun, O.; Walker, E.; Faheem, M.; Bond, J.Q.; Heyden, A. Theoretical investigation of the hydrodeoxygenation of levulinic acid to γ-valerolactone over Ru (0001). *ACS Catal.* **2016**, *7*, 215–228. [CrossRef]
47. Mamun, O.; Saleheen, M.; Bond, J.Q.; Heyden, A. Investigation of solvent effects in the hydrodeoxygenation of levulinic acid to γ-valerolactone over Ru catalysts. *J. Catal.* **2019**, *379*, 164–179. [CrossRef]
48. Yu, Z.; Lu, X.; Xiong, J.; Li, X.; Bai, H.; Ji, N. Heterogeneous catalytic hydrogenation of levulinic acid to γ- valerolactone with formic acid as internal hydrogen source: Key issues and their effects. *ChemSusChem* **2020**, *13*, 2916–2930. [CrossRef]
49. Kuwahara, Y.; Kaburagi, W.; Osada, Y.; Fujitani, T.; Yamashita, H. Catalytic transfer hydrogenation of biomass-derived levulinic acid and its esters to γ-valerolactone over ZrO_2 catalyst supported on SBA-15 silica. *Catal. Today* **2017**, *281*, 418–428. [CrossRef]
50. Yu, J.; Savage, P.E. Decomposition of formic acid under hydrothermal conditions. *Ind. Eng. Chem. Res.* **1998**, *37*, 2–10. [CrossRef]
51. Assary, R.S.; Curtiss, L.A.; Dumesic, J.A. Exploring meerwein–ponndorf–verley reduction chemistry for biomass catalysis using a first-principles approach. *ACS Catal.* **2013**, *3*, 2694–2704. [CrossRef]
52. Kumar, V.V.; Naresh, G.; Sudhakar, M.; Tardio, J.; Bhargava, S.K.; Venugopal, A. Role of brønsted and lewis acid sites on Ni/TiO_2 catalyst for vapour phase hydrogenation of levulinic acid: Kinetic and mechanistic study. *Appl. Catal. A Gen.* **2015**, *505*, 217–223. [CrossRef]
53. Mohan, V.; Venkateshwarlu, V.; Pramod, C.V.; Raju, B.D.; Rao, K.S.R. Vapour phase hydrocyclisation of levulinic acid to γ-valerolactone over supported Ni catalysts. *Catal. Sci. Technol.* **2014**, *4*, 1253–1259. [CrossRef]
54. Putrakumar, B.; Nagaraju, N.; Kumar, V.P.; Chary, K.V.R. Hydrogenation of levulinic acid to γ-valerolactone over copper catalysts supported on γ-Al_2O_3. *Catal. Today* **2015**, *250*, 209–217. [CrossRef]
55. Lomate, S.; Sultana, A.; Fujitani, T. Vapor phase catalytic transfer hydrogenation (CTH) of levulinic acid to γ-valerolactone over copper supported catalysts using formic acid as hydrogen source. *Catal. Lett.* **2018**, *148*, 348–358. [CrossRef]
56. Murugesan, K.; Alshammari, A.S.; Sohail, M.; Jagadeesh, R.V. Levulinic acid derived reusable cobalt-nanoparticles-catalyzed sustainable synthesis of γ-valerolactone. *ACS Sustain. Chem. Eng.* **2019**, *7*, 14756–14764. [CrossRef]
57. Novodárszki, G.; Solt, H.E.; Valyon, J.; Lónyi, F.; Hancsók, J.; Deka, D.; Tuba, R.; Mihályi, M.R. Selective hydroconversion of levulinic acid to γ-valerolactone or 2-methyltetrahydrofuran over silica-supported cobalt catalysts. *Catal. Sci. Technol.* **2019**, *9*, 2291–2304. [CrossRef]
58. Long, X.; Sun, P.; Li, Z.; Lang, R.; Xia, C.; Li, F. Magnetic Co/Al_2O_3 catalyst derived from hydrotalcite for hydrogenation of levulinic acid to γ-valerolactone. *Chin. J. Catal.* **2015**, *36*, 1512–1518. [CrossRef]
59. Obregón, I.; Corro, E.; Izquierdo, U.; Requies, J.; Arias, P.L. Levulinic acid hydrogenolysis on Al_2O_3-based Ni-Cu bimetallic catalysts. *Chin. J. Catal.* **2014**, *35*, 656–662. [CrossRef]
60. Yanase, D.; Yoshida, R.; Kanazawa, S.; Yamada, Y.; Sato, S. Efficient formation of γ-valerolactone in the vapor-phase hydrogenation of levulinic acid over Cu-Co/alumina catalyst. *Catal. Commun.* **2020**, *139*, 105967–105971. [CrossRef]
61. Pendem, S.; Mondal, I.; Shrotri, A.; Rao, B.S.; Lingaiah, N.; Mondal, J. Unraveling the structural properties and reactivity trends of Cu–Ni bimetallic nanoalloy catalysts for biomass-derived levulinic acid hydrogenation. *Sustain. Energy Fuels* **2018**, *2*, 1516–1529. [CrossRef]
62. He, Z.; Jiang, C.; Wang, Z.; Wang, K.; Sun, Y.; Yao, M.; Li, Z.; Liu, Z. Catalytic hydrodeoxygenation of biomass-derived oxygenates to bio-fuels over Co-based bimetallic catalysts. *Sustain. Energy Fuels* **2020**, *4*, 4558–4569. [CrossRef]
63. Yepez, A.; De, S.; Climent, M.; Romero, A.; Luque, R. Microwave-assisted conversion of levulinic acid to γ-valerolactone using low-loaded supported iron oxide nanoparticles on porous silicates. *Appl. Sci.* **2015**, *5*, 532–543. [CrossRef]
64. Hussain, S.; Velisoju, V.K.; Rajan, N.P.; Kumar, B.P.; Chary, K.V.R. Synthesis of γ-valerolactone from levulinic acid and formic acid over Mg-Al hydrotalcite like compound. *ChemistrySelect* **2018**, *3*, 6186–6194. [CrossRef]
65. Xu, S.; Yu, D.; Ye, T.; Tian, P. Catalytic transfer hydrogenation of levulinic acid to γ-valerolactone over a bifunctional tin catalyst. *RSC Adv.* **2017**, *7*, 1026–1031. [CrossRef]
66. Wang, J.; Zhang, G.; Liu, M.; Xia, Q.; Yu, X.; Zhang, W.; Shen, J.; Yang, C.; Jin, X. Lattice distorted MnCo oxide materials as efficient catalysts for transfer hydrogenation of levulinic acid using formic acid as H-donor. *Chem. Eng. Sci.* **2020**, *222*, 115721. [CrossRef]
67. Kuwahara, Y.; Kango, H.; Yamashita, H. Catalytic transfer hydrogenation of biomass-derived levulinic acid and its esters to γ-valerolactone over sulfonic acid-functionalized UiO-66. *ACS Sustain. Chem. Eng.* **2016**, *5*, 1141–1152. [CrossRef]
68. Xue, Z.; Jiang, J.; Li, G.; Zhao, W.; Wang, J.; Mu, T. Zirconium–cyanuric acid coordination polymer: Highly efficient catalyst for conversion of levulinic acid to γ-valerolactone. *Catal. Sci. Technol.* **2016**, *6*, 5374–5379. [CrossRef]
69. Yun, W.C.; Yang, M.T.; Lin, K.A. Water-born zirconium-based metal organic frameworks as green and effective catalysts for catalytic transfer hydrogenation of levulinic acid to gamma-valerolactone: Critical roles of modulators. *J. Colloid. Interface Sci.* **2019**, *543*, 52–63. [CrossRef]
70. Rai, P.K.; Kumar, V.; Lee, S.; Raza, N.; Kim, K.H.; Ok, Y.S.; Tsang, D. Nanoparticle-plant interaction: Implications in energy, environment, and agriculture. *Green Energy Environ.* **2018**, *119*, 1–19. [CrossRef]

71. Yang, Y.; Gu, L.; Guo, S.; Shao, S.; Li, Z.; Sun, Y.; Hao, S. N-doped mesoporous carbons: From synthesis to applications as metal-free reduction catalysts and energy storage materials. *Front. Chem.* **2019**, *7*, 761. [CrossRef] [PubMed]
72. Liu, L.; Gao, F.; Concepción, P.; Corma, A. A new strategy to transform mono and bimetallic non-noble metal nanoparticles into highly active and chemo selective hydrogenation catalysts. *J. Catal.* **2017**, *350*, 218–225. [CrossRef]